Review Draft

An Evaluation of Hospital Radiation Detectors for Use in Screening Potentially Contaminated Individuals

Prepared by

R. Anigstein, M. C. Erdman, S. H. King, J. J. Mauro, K. L. Miller, and R. H. Olsher

S. Cohen & Associates
6858 Old Dominion Drive
McLean, Virginia 22101

Under

Contract Number 200-2002-00367
Task Order Number 0003

Prepared for

Phillip Green
Project Officer

November 2005

Contents

Page

Tables

Page

Figures

Page

Figures (continued)

Page

Chapter 1

FIELD STUDIES OF HOSPITAL RADIATION DETECTORS

1.1 Introduction

The detonation of an improvised nuclear device or a radioactive dispersal device (RDD) would lead to wide-spread radioactive contamination, including the potential contamination of individuals. If such an event were to happen, it would be desirable to have various means of rapidly scanning individuals to determine if they have either external or internal contamination and to be able to determine when decontamination procedures have been successful. Nearly all hospitals provide nuclear medicine services for their patients. Therefore, most hospitals already possess various pieces of radiation detection equipment, including gamma cameras, thyroid uptake counters, Geiger-Mueller counters, and other portable radiation detection and measurement instruments. In addition, because of concerns over radioactivity inadvertently leaving the hospital in normal trash or over receiving patients in the emergency department who might be unknowingly contaminated with radioactive materials, a number of hospital have installed portal monitors that are capable of detecting low levels of radioactivity.

SC&A, Inc., in collaboration with the Hershey Medical Center (HMC), performed studies to determine the suitability of radiation detection and imaging systems commonly found in hospitals for rapidly scanning individuals for internal contamination. The present chapter describes field studies to evaluate the potential use of nuclear medicine gamma camera systems, thyroid uptake counters, and portal monitors for detecting and measuring low levels of internal contamination. Chapter 2 describes the use of computer models to simulate the response of two models of gamma cameras to radionuclides distributed in the lungs of an anthropomorphic phantom based on Reference Man.

1.2 Materials and Equipment

1.2.1 Phantoms for Use with Discrete Radioactive Sources

Various phantoms were potentially available for this study, including a Rando Phantom,[1] and a chest and torso phantom[2] used in the nuclear power industry for whole body counting (see Figure 1-1). However, these phantoms could not be loaded with the readily available sources used for these measurements without permanently altering the phantom, such as by drilling larger holes, which made them unsuitable for use in the present study. To obviate these difficulties, a simplified phantom was constructed from slabs of poly(methyl methacrylate) (PMMA), a clear plastic commonly known as acrylic and sold under various brand names, including Plexiglas®, Lucite®, and Acrylite®. PMMA has the empirical chemical formula

[1] The Phantom Laboratory, Salem, NY.

[2] Phantom courtesy of the Health Physics staff at the Three Mile Island Nuclear Power Station, Middletown, PA.

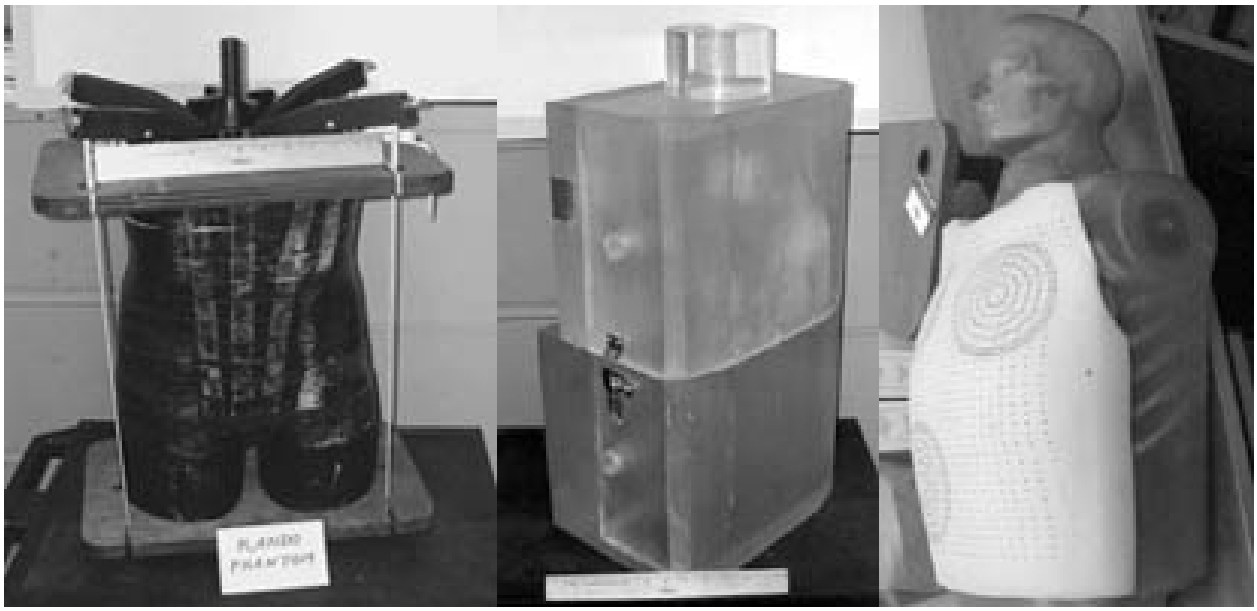

Figure 1-1. Examples of Phantoms Used in Radiation Measurements

$(C_5O_2H_8)_n$ and a typical density of 1.19 g/cm^3.

Prior to adopting the acrylic phantom, its radiation absorption properties were compared to equal thicknesses of the Rando Phantom. When the results showed that the two materials produced the same attenuation, the acrylic phantom was chosen for use in the present study. The phantom consists of a series of identical slabs, each 11.75 × 11.75 inches (29.85 × 29.85 cm), with a nominal thickness of $\frac{15}{16}$ in (2.38 cm). Up to ten of these slabs were used to simulate varying thicknesses of tissue between the radiation source and the detector. The source, embedded in an acrylic disc, was mounted at the center of an 11th slab. This source slab was identical to the others except for a hole in the center that is 1.125 inches in diameter and 0.375 inch deep (2.86 × 0.95 cm). A schematic view of the components of the phantom is presented in Figure 1-2; a photograph of the assembled phantom, comprising all 11 slabs, is shown in Figure 1-3. The hole for the disk source is visible in the photograph in the third slab from the right.

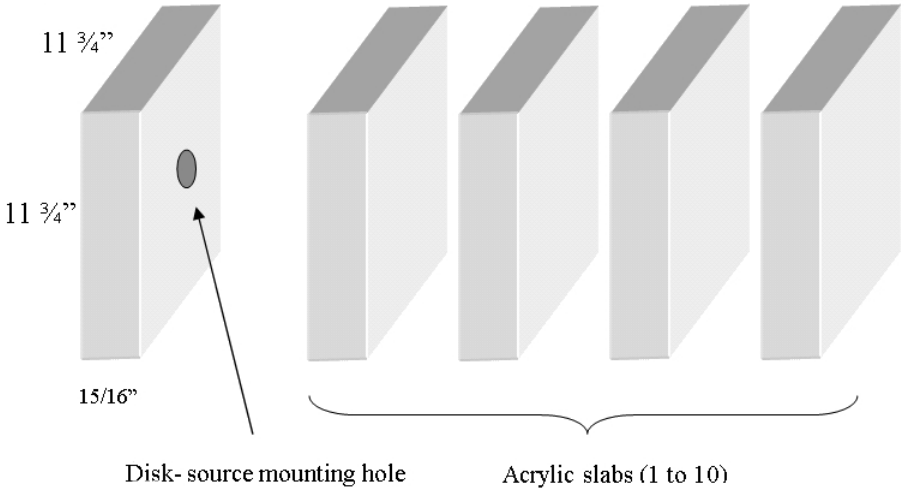

Figure 1-2. Acrylic Phantom: Schematic View of Components

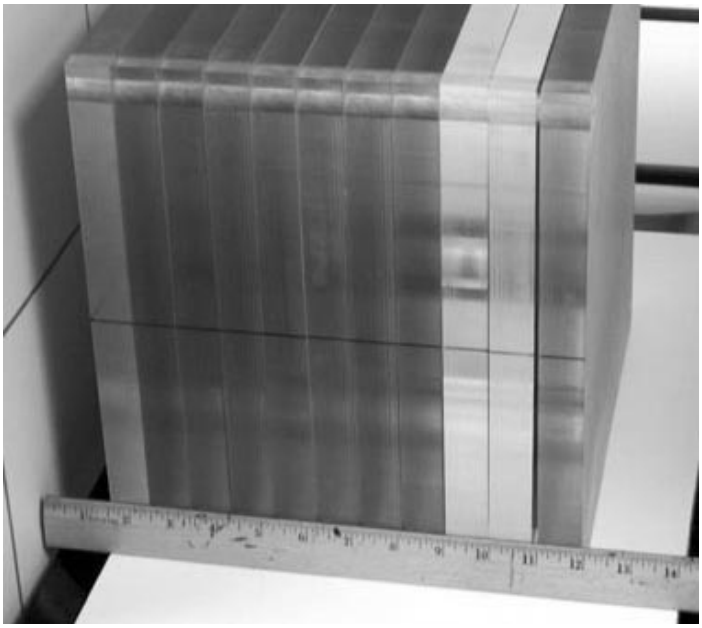

Figure 1-3. View of Assembled Acrylic Phantom

Figure 1-4. Water-Filled Phantom

Phantom for Distributed Source

A water-filled container was used to compare the count rates from a discrete source, such as the ones used in the present study, and a source distributed over a volume that would correspond to a region of the human body. The container was a plastic jug, 28 × 16 cm by 38 cm high, filled with water to a depth of 34 cm (see Figure 1-4). ^{131}I was chosen for use in this comparison because it is readily available in aqueous solution and is commonly used in nuclear medicine. A discrete source was represented by an ampule containing ^{131}I that was placed in a plastic test tube filled with water and suspended in the water-filled jug by a wire at the center of the container. To measure the count rates from a distributed source, the ampule was broken and the jug thoroughly shaken, uniformly distributing the activity throughout the volume of water.

1.2.2 Radioactive Sources

The four radionuclides that were the principal focus of this study—^{60}Co, ^{137}Cs, ^{192}Ir, and ^{241}Am—were selected from among those likely to be used in an RDD and that emit γ rays that span a wide range of energies. NIST-traceable sealed sources of ^{60}Co and ^{137}Cs were obtained from Isotope Products Laboratories, while NIST-traceable sources of ^{241}Am came from North American Scientific. Sources of each of these three radionuclides were procured with nominal activities of 1 or 10 μCi (37 or 370 kBq). Each of the ^{60}Co and ^{137}Cs sources consists of evaporated salts that were deposited at the bottom of a cylindrical cavity in an acrylic disk; the cavity was then plugged with an epoxy resin. The source comprises a thin disk, 5 mm in diameter, 2.77 mm from the face of the acrylic disk. The ^{241}Am source is in the form of a resin bead, 1 mm in diameter, mounted 1 mm from the surface of the disk. The source configurations are illustrated in Figures 1-5 and 1-6.

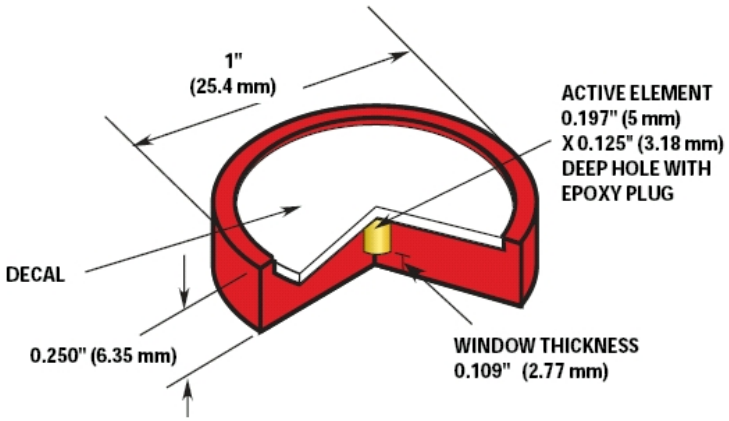

Figure 1-5. ^{137}Cs and ^{60}Co Sources (IPL 2003)

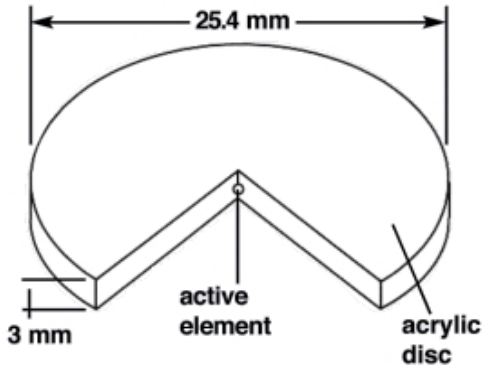

Figure 1-6. ^{241}Am Sources (NAS 2005)

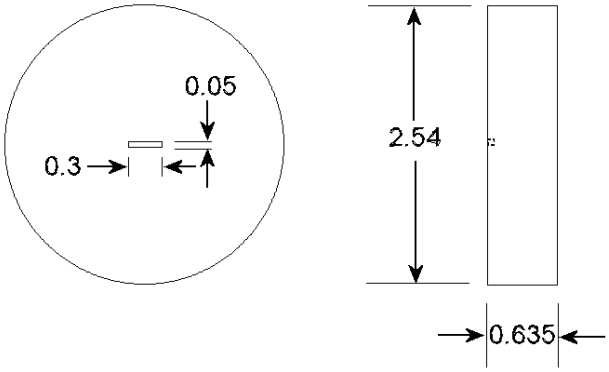

Figure 1-7. Source Holder for ^{192}Ir (dimensions in cm)

^{192}Ir was not readily available as a NIST-traceable source. However, a relatively low-activity ^{192}Ir source was obtained in the form of a spent radiation therapy seed, with a strength of approximately 41 µCi, which decayed to about 18 µCi (~670 kBq) by the time of the experiments. The seed consisted of a 0.3-mm diameter core of 10% Ir–90% Pt, sealed inside a 0.1-mm-thick cylindrical platinum shell, 0.5 mm in outer diameter and 3 mm long. The shell was mounted lengthwise inside an acrylic disk to emulate as closely as possible the configuration of the NIST-traceable sources (see Figure 1-7). In addition to the sealed sources, ^{131}I was obtained in aqueous solution, as discussed on page 1-3. This source had an initial activity of 56 µCi (~2.1 MBq).

Detailed information on the sources and some of their radiological properties are presented in Table 1-1.

1.2.3 Gamma Cameras

The nuclear medicine gamma camera is also known as the Anger camera, after its inventor, Hal Anger. The following description is adapted from Amersham 2004:

> The camera consists of a collimator placed between the detector surface and the patient. The collimator is made of a lead alloy and serves to suppress γ rays which deviate substantially from a direction perpendicular to the detector. The detector is a single crystal of thallium-doped sodium iodide (NaI[Tl]), which produces a flash of scintillation light when an impinging γ ray or x ray interacts with the crystal. (Hence the name "scintillation camera" that is sometimes applied to this instrument.) The intensity of the scintillation is proportional to the energy of the incident photon. This light is detected by an array of photomultiplier tubes (PMTs) that are optically coupled to the surface of the crystal. The output signal from

the PMTs is an electrical pulse that is proportional to the intensity of the light and hence to the energy of the incident photon. The PMTs are variably activated, depending on the position of the event in the crystal. The entire system response thus yields positional information which can be recorded on photographic film, using an analogue output, or as a digital image that is stored in a computer coupled to the camera.

Table 1-1. Radioactive Sources Used in Study

Nuclide		Co-60	I-131	Cs-137	Ir-192	Am-241
Activity (μCi)	Source 1	1.007	56.03	0.9561	40.8	1.065
	Source 2	10.2		9.745		9.102
Assay date		11-1-04	11-18-04	11-1-04	10-18-04	1-1-05
Supplier[a]		IPL	NAS	IPL	Alpha-Omega	NAS
NIST-traceable?		Y	Y	Y	N	Y
Active diameter (cm)		0.5	N/A	0.5	N/A	0.1
Window	Material	Acrylic	N/A	Acrylic	Pt	Acrylic
	Thickness (cm)	0.277	N/A	0.277	0.05	0.1
Diameter of holder (cm)		2.54	N/A	2.54	2.54	2.54
Thickness of holder (cm)		0.635	N/A	0.635	0.635	0.3
Half-life		5.27 y	8.02 d	30.07 y	73.83 d	432.2 y
Principal γ-rays	Energy (keV)	1173.2 1332.5	364.5	661.7	296.0 – 612.5	59.5
	Intensity	1.000 1.000	0.817	0.851	2.129[b]	0.359

[a] NAS: North American Scientific, 20200 Sunburst Street, Chatsworth, CA 91311, http://www.nasmedical.com
IPL: Isotope Products Laboratories, 24937 Avenue Tibbitts, Valencia, CA 91355, http://www.isotopeproducts.com
Alpha Omega Services, Inc., 9156 Rose Street, Bellflower, CA 90706, http://www.alpha-omegaserv.com/

[b] Total intensity of all γ radiation in this energy range

The NaI(Tl) crystals in gamma cameras currently on the market range in thickness from ⅜-inch (0.95 cm) to 1 inch (2.5 cm). The thickness of the crystal can affect the detection efficiency of the system. High energy photons, such as those characteristic of ^{137}Cs and ^{60}Co, are more efficiently captured and detected by the thicker crystals. However, most current nuclear medicine diagnostic procedures use radionuclides that emit lower energy photons—the most common radionuclide used in nuclear medicine is ^{99m}Tc, which has a principal γ-ray energy of 140.5 keV. A ⅜-inch crystal has adequate sensitivity in this energy range, and is the one most commonly found in current gamma cameras.

Hershey Medical Center has six gamma cameras produced by Philips Medical Systems, N. A. These cameras comprise two models—the AXIS and the SKYLight—which are illustrated in Figures 1-8 and 1-9. Four of the HMC cameras have ⅜-inch (0.95-cm) NaI(Tl) crystals and two have ¾-inch (1.9 cm) crystals. The AXIS camera, shown in Figure 1-8, has a field of view of 15.5 × 21 in (39.3 × 53.3 cm), while that of the SKYLight, shown in Figure 1-9, is 15 × 20 in

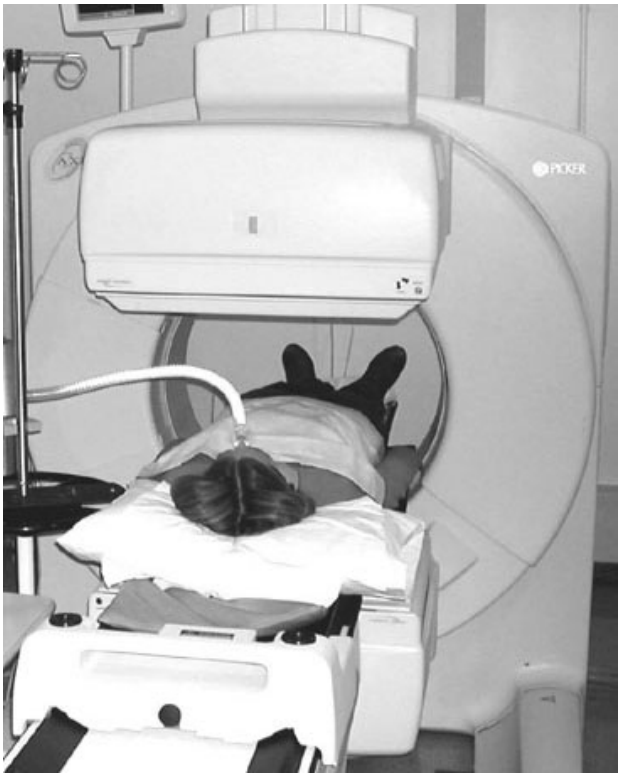

Figure 1-8. Philips AXIS Camera

Figure 1-9. Philips SKYLight Camera

(38.1 × 50.8 cm).[3] Two different camera systems were used in the present study: an AXIS system with a ¾-inch crystal, and a SKYLight system with a ⅜-inch crystal. Most of the studies were performed on the AXIS system; the SKYLight studies were limited to the investigation of discrete and distributed sources in the water-filled phantom seen in Figure 1-9.

Both the AXIS and SKYLight cameras have dual-head detector systems that allow the detector heads to be positioned at varying angles about the patient. The AXIS uses the conventional type of gantry on which the detector heads are mounted that allows the heads to be positioned at any angle about the patient, who typically lies on a table along the central axis of the detector gantry. The SKYLight system represents a newer design in which each detector head can be positioned independently of the other. Each camera system's computer performs acquisition, processing, display, archiving, and networking of the nuclear medicine data. The data in the present study consist of count rates from one detector head at a time. In actual clinical practice, both detectors could be used to provide additional information.

Collimators

Collimators on gamma cameras and other radiation detectors used in nuclear medicine perform a function analogous to that of the glass lens in an optical camera. Radiation originating in

[3] This is the field of view of the collimators, which are used for imaging in normal clinical practice. With the collimator removed, the field of view of the AXIS crystal is 16 × 21.5 in (40.7 × 54.7 cm).

discrete regions of the body is directed to corresponding areas of the crystal. The scintillation light emitted in the crystal at the point a photon is absorbed or scattered forms a short-lived image which is recorded by the PMTs and the associated electronics and computer system. This image is used to create a map of the distribution of radionuclides in the region of interest—the organs or portions of the body that are the subject of the study.

Collimators on the AXIS system are made of a 95%-5% lead-antimony alloy. The collimator is a flat plate, about 1 inch (~2.5 cm) thick, that is placed against the NaI(Tl) crystal. It has a core that consists of a honeycomb of parallel holes.[4] Photons that are normally incident on (i.e., perpendicular to) the plane of the collimator pass through the holes and are recorded as part of the image. Photons striking at an oblique angle are absorbed by the collimator or scattered away from the crystal. The design of the collimator is dictated by the γ-ray energies of the radionuclides used for a given imaging study. Higher energies require thicker collimators with thicker septa (the separations between the holes).

Several collimators are available for each type of camera system, including low-energy (< 200 keV), medium-energy (200 – 400 keV), high-energy (400 – 600 keV), and pinhole collimators. The collimators used in most routine diagnostic studies are the low-energy type, often referred to as the Low Energy All Purpose (LEAP) collimator (see Figures 1-10 and 1-11). The LEGAP collimator used with the AXIS camera is of this type, as is the LEGP collimator used with the SKYLight.

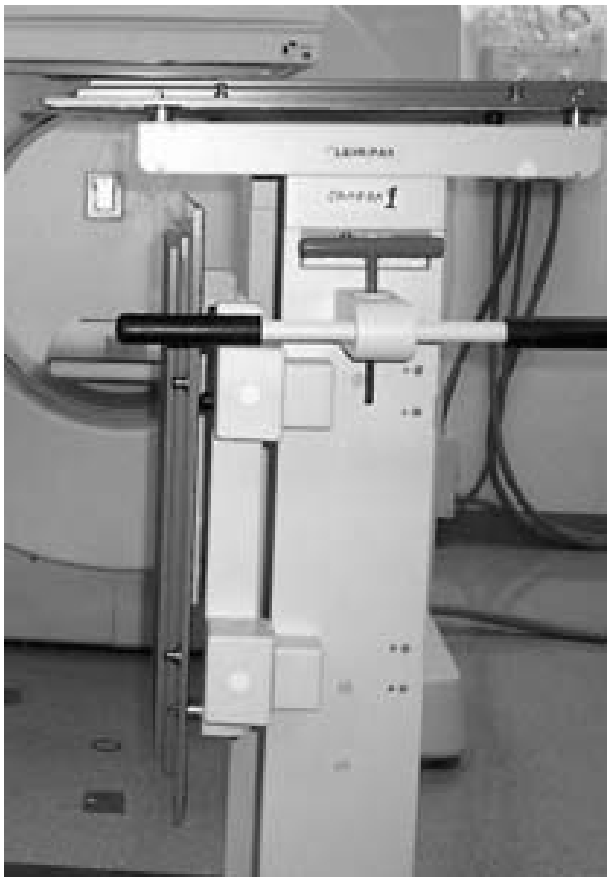

Figure 1-10. Collimators in Rack

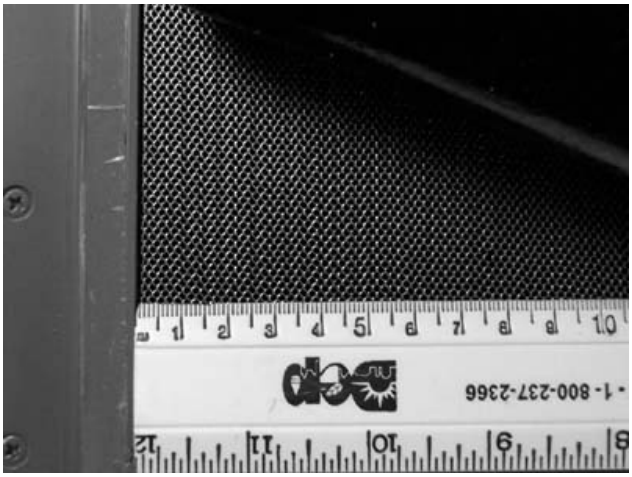

Figure 1-11. Back of Collimator Showing Corrugated Lead Strips

[4] Parallel holes produce an image that has the same size as the region of interest. Collimators with divergent-convergent holes can be used to enlarge or reduce the image.

Collimators enable gamma cameras to image the distribution of radionuclides in the body, the main function of these instruments in nuclear medicine. However, in the contemplated use of these instruments to screen individuals who were exposed to airborne radioactive materials, collimators, which by design have a narrow angle of acceptance, would shield out most of the photons and thus decrease the sensitivity of the detector system. Removal of the collimator improves the sensitivity of the camera; however, it also increases the background count rate. Since the minimum detectable activity (MDA) is a function of both the counting efficiency and the background count rate, we studied the response of the cameras both with and without collimators to determine the MDAs and thus the optimum use of the systems for the contemplated purpose.

Pulse Height Analyzer

The typical radionuclide used in nuclear medicine emits a principal γ ray with a single energy that is used for imaging the distribution of that nuclide in a patient. When a γ ray interacts with the NaI(Tl) crystal, the average intensity of the resulting scintillation is proportional to the energy of the incident photon. The electrical signal produced by the PMTs is in turn proportional to the scintillation. However, because of variations in the efficiency of converting the γ-ray energy to light, as well as in the efficiency of converting the scintillation to an electrical pulse, even monoenergetic γ-ray photons produce a spectrum of pulses.

In addition to the distribution of pulse heights corresponding to the direct interaction of the γ ray with the NaI(Tl) crystal, the spectrum also includes events of lower energies. These include the escape peak—the energy deposited in the crystal when an iodine K-shell x ray (which has an average energy of 29 keV) escapes from the crystal. The energy of the escape peak is therefore 29 keV lower than the photopeak energy. More prominently, lower-energy pulses are generated when γ rays undergo Compton scattering in the patient's body, or in the collimator or other parts of the camera housing. The pulses from these lower-energy photons would contribute noise in the image being generated by the camera; electronic noise in the system also generates pulses in the low-energy end of the spectrum. The camera system utilizes discriminator circuitry that can be adjusted to reject pulses outside the energy range of the γ rays from the radionuclides used for a particular study.

To help the operator determine the appropriate discriminator settings, the camera system incorporates a pulse height analyzer (PHA) that is used to display the pulse height spectrum, as shown in Figure 1-12. The scale on the PHA screen is set to display the energies of the corresponding γ rays. The screen also shows the upper and lower limits of the energy window—the range of pulse heights that will be accepted by the discriminator. The energy range is normally centered on the primary photopeak(s) of the radionuclide of interest. The width is typically set to equal 20% of the photopeak energy, meaning that pulses corresponding to energies ± 10% of the true γ-ray energy are accepted by the PHA. The camera system includes factory-installed energy windows corresponding to radionuclides commonly used in nuclear medicine. Some of the preset energy windows found in the AXIS system are shown in Table 1-2.

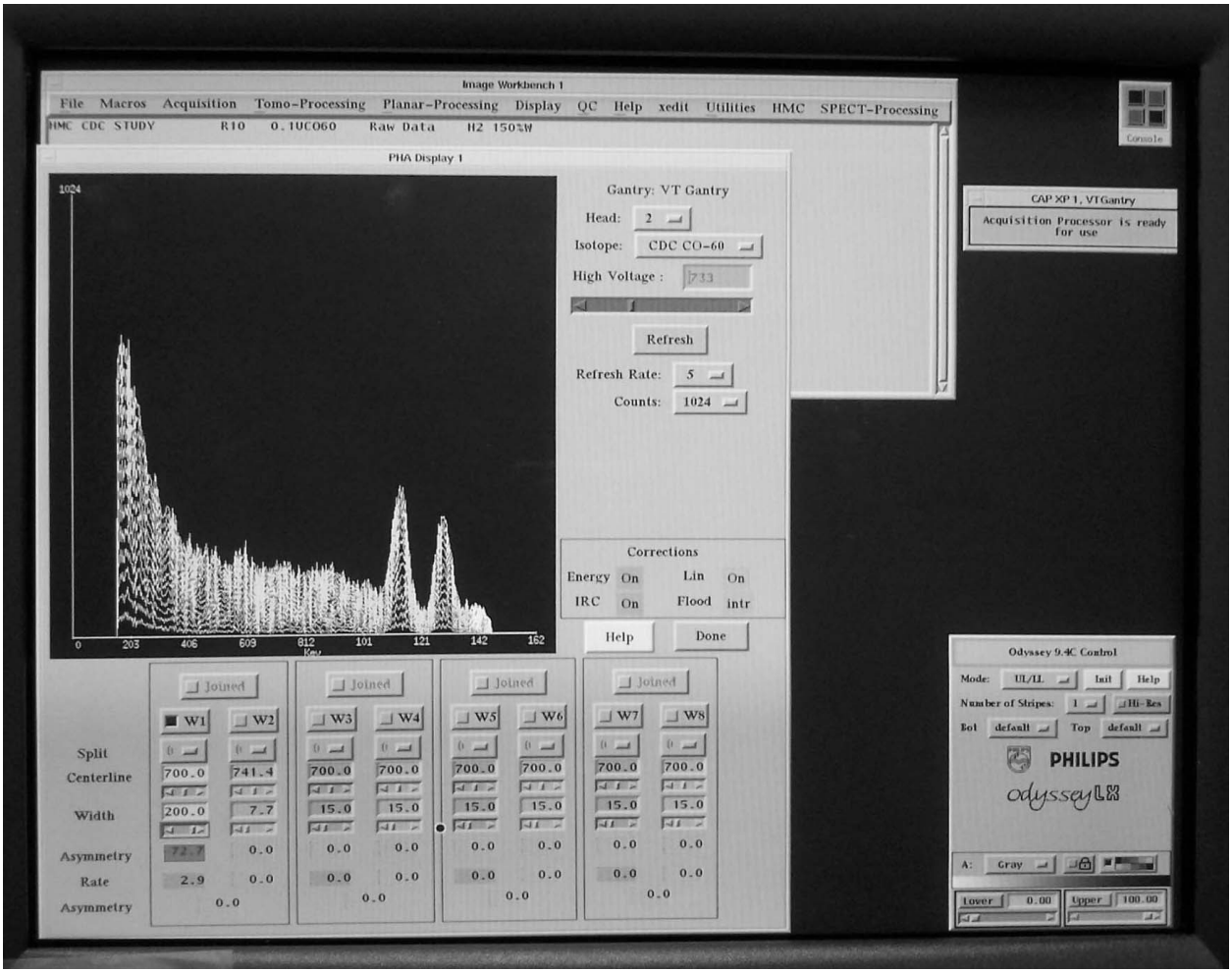

Figure 1-12. PHA screen on AXIS camera display console, showing ^{60}Co spectrum

Table 1-2. Some Preset Radionuclide Energy Windows in the AXIS Camera System

Nuclide	Peak Energy (keV)	Window (%)	Energy Range (keV)
F-18	511	20	408.8 – 613.2
Co-57	121.9[a]	15	103.6 – 140.2
Tc-99m	140.5	15	119.4 – 161.6
I-131	364	20	291.2 – 436.8
Xe-133	81	20	64.8 – 97.2
Tl-201	75	40	45.0 – 105.0

Source: Marconi Medical Systems, Inc. 2001

[a] Actual γ energy: 122.06 keV

Other radionuclide windows can be programmed into the camera's computer. The operator has ready access to the predefined energy settings in the setup menu for each patient's diagnostic acquisition. It is usually possible for him or her to alter the energy range for these preset

radionuclide windows. It is *sometimes* possible for the operator to enter custom (i.e. user-defined) windows for radionuclides that do not appear on the factory-installed list, and save these as new radionuclide windows. On the AXIS camera, the procedure to add a new radionuclide is fairly straightforward. On the SKYLight camera system, adding a new radionuclide or modifying the energy range for an existing radionuclide requires password access to the Administrator section of the computer system. This section is rarely used by technologists or field engineers, so the password may not be commonly known. In either case, temporary adjustments to the centerline energy and the window width may be possible if the technologist is sufficiently familiar with the camera system.

In the AXIS camera system, the maximum peak energy—the energy that would normally correspond to the photopeak or the center of the photopeaks of the nuclide in question—that can be set in the PHA is 700 keV. However, photons with higher energies can be counted if they fall within the energy window. The highest energy can be achieved by setting the photopeak to 700 keV and the window width to "200%." This designation is a shorthand reference to the actual energy window. To understand this setting, we note that the PHA displays a histogram of the pulse height spectrum. The scale can be expressed in channels (arbitrary binning units). For display purposes, the range is 0 – 256 on the horizontal axis. For a nuclide with a single γ ray, the centerline of the photopeak is set to Channel 110. Only pulses in Channels 25 – 231 are displayed and counted by the system. Thus, with the centerline of the "200%" window set to 700 keV, the maximum energy, which corresponds to Channel 231, is 1470 keV (700 × 231 ÷ 110 = 1470), while the minimum energy, corresponding to Channel 25, is 159 keV. Thus, ^{60}Co, with principal γ-ray energies of 1173.4 and 1332.5 keV, falls within this energy window. The entire ^{60}Co spectrum, including the two principal photopeaks and the lower-energy Compton-scattered photons, is visible in the display in Figure 1-12. The AXIS camera, if properly adjusted, can thus be used to detect and identify all the radionuclides in the present study.

The PHA of the SKYLight camera system can be set to encompass energies up to 920 keV. This enables the system to record the principal photopeaks for ^{131}I, ^{137}Cs, ^{192}Ir, and ^{241}Am. However, in the case of ^{60}Co, only Compton-scattered photons with energies < 920 keV can be counted.

Many of the radionuclides that are likely to be used in an RDD are not included in the list of factory-installed energy windows on gamma cameras. However, predefined energy windows can usually be adjusted to encompass the gamma spectrum for these radionuclides. Rather than define a new radionuclide as a custom addition, it may be easier to utilize radionuclides in the predefined list and simply expand the acquisition width to encompass the photopeaks of the nuclide of interest. Table 1-3 lists the radionuclides addressed by the present study and the settings used in the experiments reported in this chapter.

1.2.4 Thyroid Uptake System

The Hershey Medical Center's Atomlab 950 Thyroid Uptake System, made by Biodex Medical Systems, Inc., is typical of the thyroid counting systems used in nuclear medicine departments. This system, shown in Figure 1-13, consists of a 2 × 2 in (5 × 5 cm) NaI(Tl) detector coupled to

Figure 1-13. Atomlab 950 Thyroid Uptake System

a 1024-channel multi-channel analyzer (MCA), shown in Figure 1-14. The MCA, analogous to the PHA on the Philips gamma cameras, has factory-installed settings for approximately 23 radionuclides, and can accept 50 additional user-defined nuclides. The preprogrammed nuclides include ^{60}Co, ^{131}I, ^{137}Cs, and ^{192}Ir. For the purpose of the present study, ^{241}Am was added to the MCA radionuclide database, with a photopeak energy of 60 keV and an energy window with a range of 15 to 75 keV.

Table 1-3. AXIS Camera Parameters Used for Radionuclides in Present Study

Actual Radionuclide	Principal γ-ray Energies (keV)	Preset Radionuclide	AXIS Energy Window	
			%	keV
Co-60	1173.2, 1332.5	Cs-137	20	595 – 728
			100	331 – 992
Cs-137	661.7	Cs-137	20	595 – 728
Ir-192	296.0 – 612.5	F-18	100	256 – 767
Am-241	59.5	Xe-133	100	40.5 – 121.5

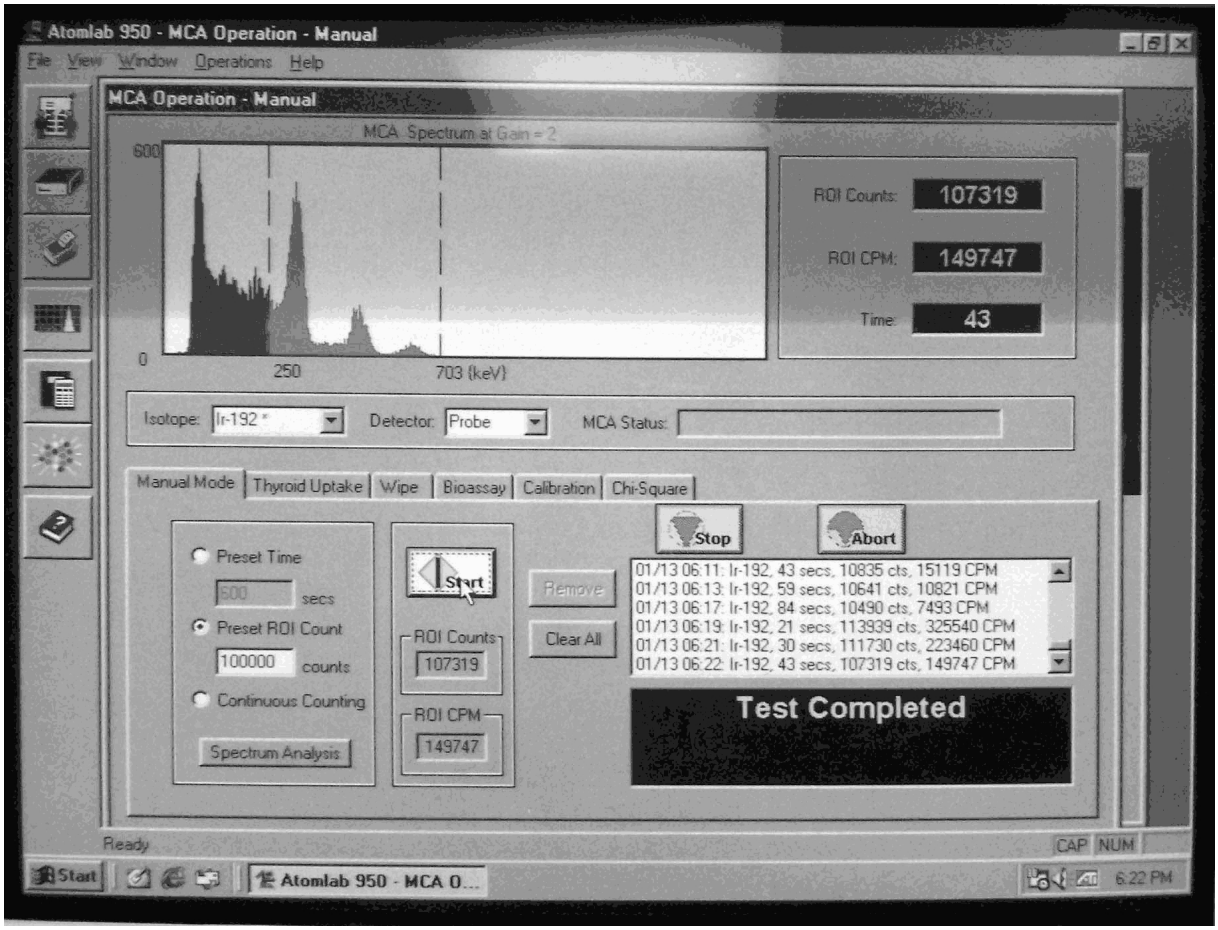

Figure 1-14. Atomlab 950 MCA Screen Showing Highlighted Region with ^{192}Ir Photopeaks

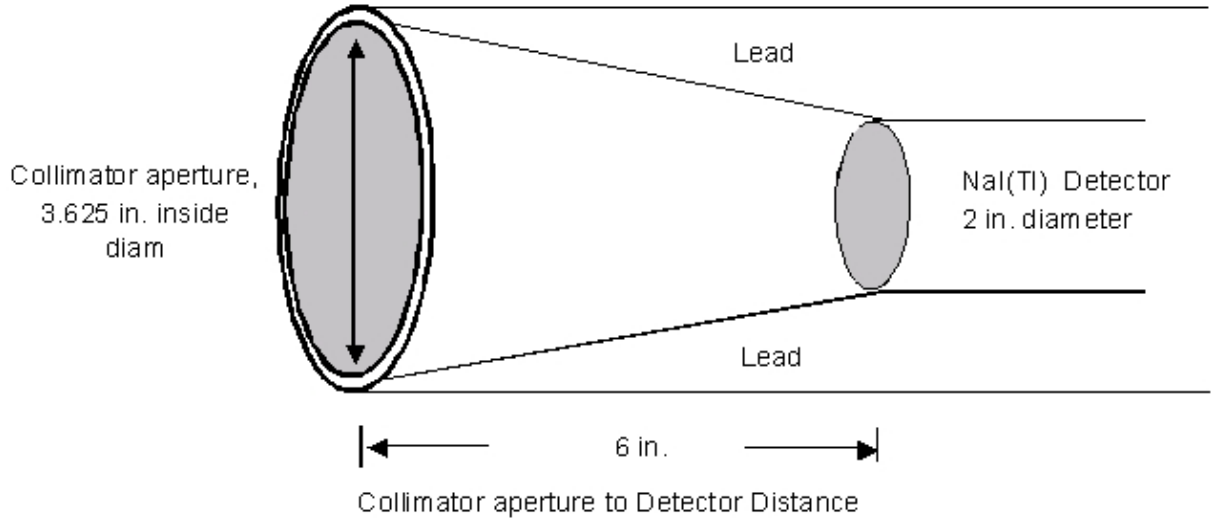

Figure 1-15. Schematic Diagram of Collimator on Atomlab Thyroid Uptake Probe

The NaI(Tl) detector is typical of detectors on thyroid counting systems, and is shielded with a conventional flat-field lead collimator that meets IAEA specifications. The design of the collimator and the position of the NaI(Tl) crystal are shown in the schematic diagram in Figure 1-15. The inside diameter of the front edge of the collimator is approximately 3.6 in (9.1 cm), with a thickness of about 0.2 in (0.48 mm) on the outer rim. The cavity inside the collimator is in the shape of a 6-in-long (15.2 cm) truncated cone. The base of the cone is 3.625 in (9.2 cm) in diameter, while the opposite face has a diameter of 2 in (5.1 cm). The remaining dimensions are shown in the diagram. The collimator shields both the detector and the PMT, minimizing the effects of background radiation. In Figure 1-13, the probe is pointed in a horizontal direction for use with patients who are sitting upright. In the orientation shown in the Figures 1-13 and 1-15, the detector is facing left.

1.2.5 Portal Monitor

Hershey Medical Center uses a Ludlum Model 375-30 Waste Monitor as a portal monitor. This monitor includes a pair of NaI(Tl) crystals, 1 inch thick by 3 inches in diameter (~2.5 × 7.6 cm), that face each other across a doorway. The detectors are shielded by a 0.71-in (1.8-cm) layer of lead. Each detector assembly is mounted on an independent frame that is mounted on wheels (see Figure 1-16). The detectors share a single digital alarming rate meter (Ludlum Model 375 Digital Area Monitor). A Star DP8340 dot matrix printer is attached to the rate meter's serial output. In addition to the printer log, each alarm trip produces an audible alarm. At HMC, this system is located in a corridor through which all trash and laundry carts must pass on their way from the hospital portion of the facility to the processing area. The cabinet openings are fitted with acrylic panels to prevent unauthorized access to the electronics and the detector mounting bolts. The distance separating the two detectors is approximately 80 inches (2 m). Because of the protective panel, the closest normal approach to either detector is 4.5 cm.

Figure 1-16. Detector Assembly of the HMC Portal Monitor

The system is located one floor below ground level. The background radiation at this location was measured to be 2.5 to 3.0 µR/h from both detectors combined, and approximately 1.5 µR/h with only one detector connected. An alarm set point of 10 µR/h is normally used with this system. This set point corresponds to 3 – 4 times background and

was chosen to minimize alarms due to small variations or spikes in the noise level of the instrument. According to the manufacturer's specifications, the response time of the Model 375 rate meter is typically 3 s from 10% to 90% of the final reading. When a ^{99m}Tc source was placed in the center of a loaded trash or laundry cart, shielding effects from the plastic trash and laundry carts used at this facility were found to be negligible. Through experimental measurements it was determined that the detector sensitivity for ^{99m}Tc at the center of a trash cart placed midway between the detectors is approximately 11 μCi (~400 kBq).

The simultaneous use of both detectors provides greater sensitivity and allows for patients to be directed through the doorway containing the detectors. To facilitate the analysis and interpretation of data collected in the present study, radiation measurements were performed with only one detector connected.

1.3 Radiation Measurements

1.3.1 Gamma Cameras

Sources in Air
Count rates were recorded by the AXIS camera from sources in air at various distances from the detector. Figure 1-17 shows the source, suspended from a meter stick, between the two heads of the AXIS camera. The collimator was removed from the head on the left. Figure 1-18 shows the acrylic phantom in position between the detector heads—the head on the left has the collimator in place. The 1-inch button source is shown mounted in the outermost slab of the phantom.

^{137}Cs. Figure 1-19 shows the normalized count rates of the AXIS camera with a ¾-inch crystal, with and without the LEGAP collimator, from a nominal 1 μCi ^{137}Cs source in air. The counts from the source, as well as background counts, were collected over a 2-minute interval, using the energy setting listed in Table 1-3. The count rates, with the background subtracted, are normalized to a unit activity of the source, based on the decay-corrected source activity at the time of the experiment. The change in count rate as a function of distance from the detector is primarily a function of the solid angle subtended by the exposed area of the NaI(Tl) crystal at the position of the source, and to a much smaller extent to the attenuation by the air between the source and the detector. With the collimator in place, the count rate is reduced by a factor of 5, due to the absorption and scattering of photons by the collimator. Any low-energy Compton-scattered photons that may have reached the NaI(Tl) detector were rejected by the 20% energy window and were thus not counted.

^{60}Co. Count rates of the AXIS camera from a nominal 1 μCi ^{60}Co were recorded using methods similar to those used for the ^{137}Cs determinations. The study utilized the two energy windows listed in Table 1-3. One set of count rates used the window centered on the ^{137}Cs photopeak but

Figure 1-17. AXIS Camera Showing Source Suspended from Meter Stick

with a 100% window.[5] The experiment was repeated with a 20% window centered on the same photopeak, thus reproducing the conditions used in the ^{137}Cs source measurements. Since neither of the energy ranges encompassed the two principal ^{60}Co γ rays, the recorded counts were due entirely to the Compton-scattered photons that were generated when the primary photons interacted with various materials, primarily the lead shielding in the two detector heads. These results are shown in Figure 1-20. The 20% energy window registered about one fifth of the count rate of the 100% window, indicating that the Compton spectra were more-or-less uniformly distributed over this energy range. Unlike its effect on ^{137}Cs count rates, the collimator reduced the ^{60}Co rates by less than a factor of 2 in both energy windows. This is partly because of the greater penetrating power of the ^{60}Co γ rays, and also because the collimator contributes to the buildup of the Compton-scattered photons that are recorded in these windows.

[5] Instructions for setting the "200%" window were not obtained from Philips Medical Systems until after this study was completed.

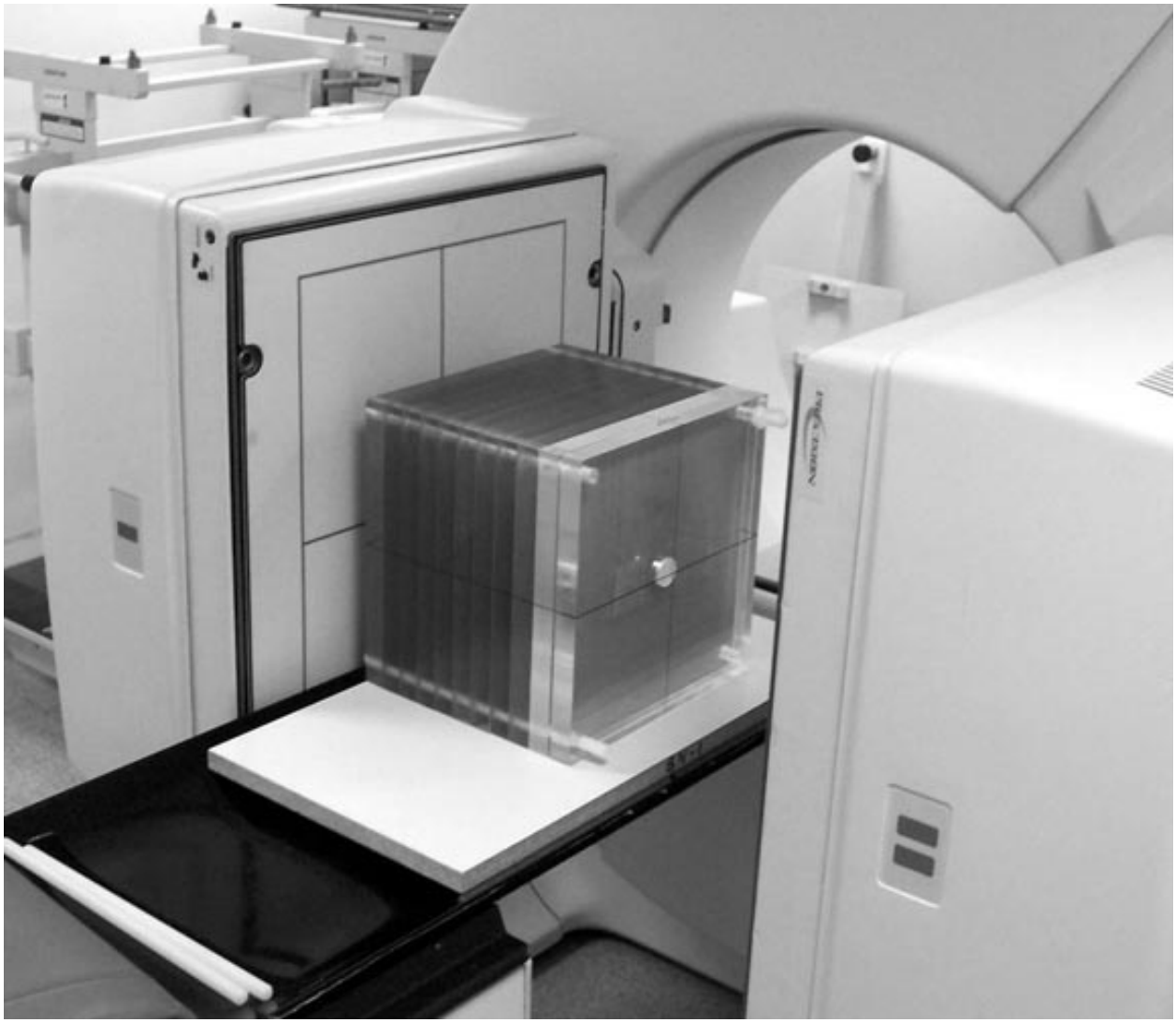

Figure 1-18. AXIS Camera Showing Source Mounted in Acrylic Phantom

^{241}Am. Count rates were recorded on the AXIS camera from ^{241}Am sources with nominal activities of 1 and 10 μCi. Figure 1-21 presents the normalized count rates, collected in a 100% ^{133}Xe window (see Table 1-3). This energy range was selected because ^{133}Xe is commonly used in nuclear medicine imaging procedures; consequently, the settings for this radionuclide are programmed into most gamma cameras, unlike those for ^{241}Am. The principal γ-ray energy of ^{133}Xe is 81 keV; expanding the width of the ^{133}Xe window to 100% results in an energy range of 40 to 122 keV, thus encompassing the principal ^{241}Am γ ray, which has an energy of 59.5 keV. However, with the LEGAP collimator, the net count rate was less than background. A gamma camera with a collimator does not appear to be an appropriate instrument for the assessment of exposure to ^{241}Am.

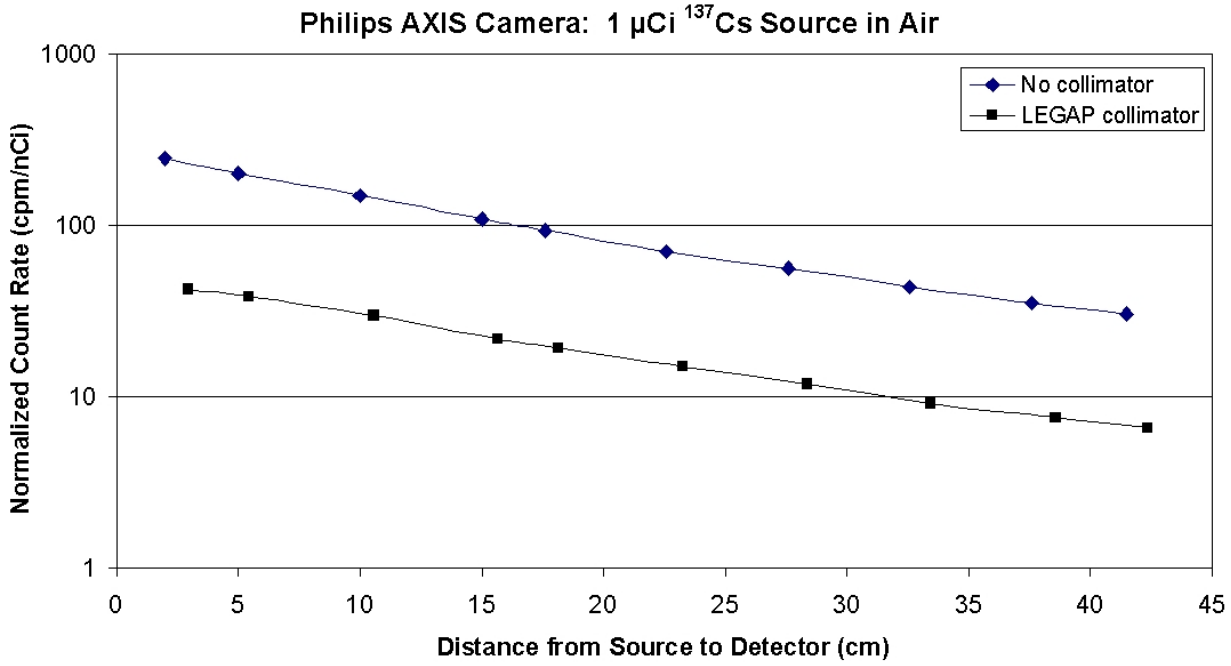

Figure 1-19. Normalized Count Rates in AXIS Camera from ^{137}Cs in Air

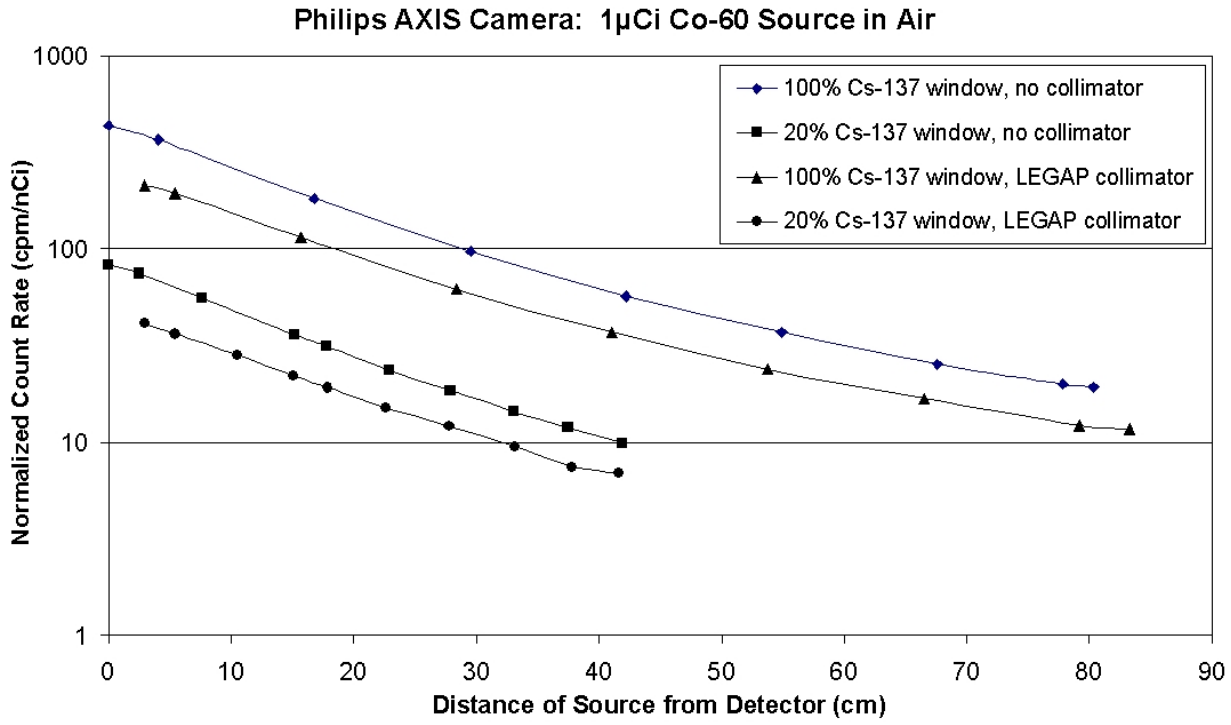

Figure 1-20. Normalized Count Rates in AXIS Camera from Co-60 Source in Air

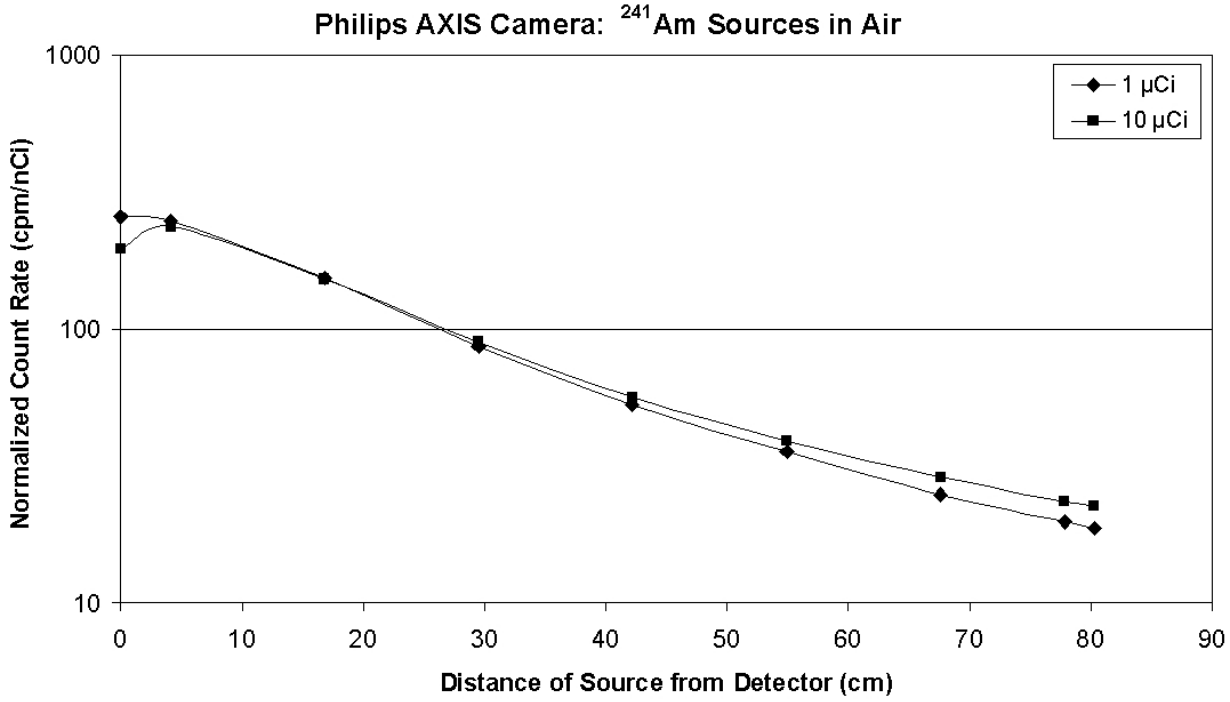

Figure 1-21. Normalized Count Rates in AXIS Camera from ^{241}Am Sources in Air

^{192}Ir. Figure 1-22 presents the normalized count rates in the AXIS system from a discrete source of ^{192}Ir, with an activity of approximately 18 µCi at the time of the measurements, counted in a 100% ^{18}F energy window, as listed in Table 1-3. As is the case for ^{241}Am, ^{192}Ir is not used for nuclear medicine imaging studies and is therefore not normally programmed into the gamma cameras. The ^{18}F window, expanded to 100%, has an energy range of 255 to 766 keV. This range encompasses over 91% of the complex γ-ray spectrum of ^{192}Ir. The LEGAP collimator reduces the count rates by about an order of magnitude.

Sources in Acrylic Phantom

Count rates were recorded on the AXIS camera from sources at different depths within the acrylic phantom. In the first set of experiments, the phantom was placed with its front face 7.6 cm from the face of the detector window, with no collimator. ^{60}Co, ^{137}Cs, and ^{241}Am sources with nominal activities of 1 µCi were placed in successive positions within the phantom. The minimum absorber between the source and the detector was the aluminum window on the detector plus the thin acrylic window on the 1-inch disk source (see page 1-4) while the maximum included the total thickness of the acrylic phantom—about 26 cm. The same energy windows were used as in the in-air measurements, except that only the 100% ^{137}Cs window was used to record counts from the ^{60}Co source.

The resulting normalized count rates are presented in Figure 1-23. The first point on the left end of each curve represents the source with minimum attenuation. Each successive point corresponds to an additional 2.4-cm-thick slab of acrylic. The total thickness of the attenuating acrylic phantom can be determined from subtracting the 7.6-cm air gap between the phantom

and the detector from the distance between the source and the detector that is listed on the X-axis.

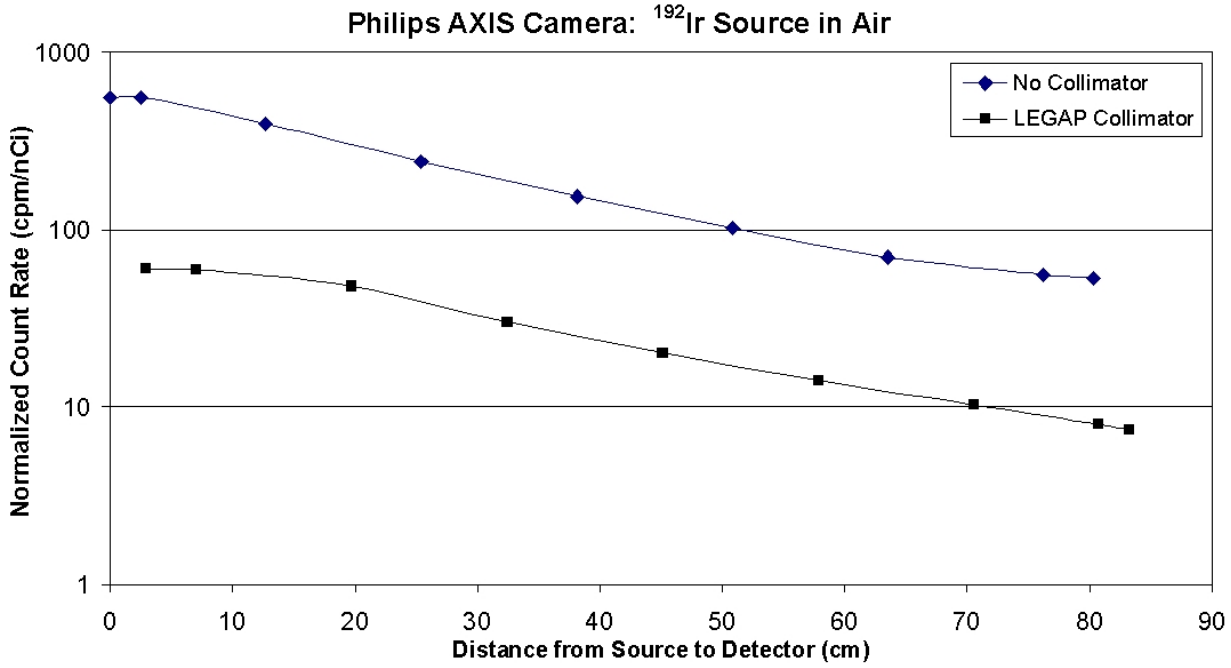

Figure 1-22. Normalized Count Rates in AXIS Camera from ^{192}Ir Source in Air

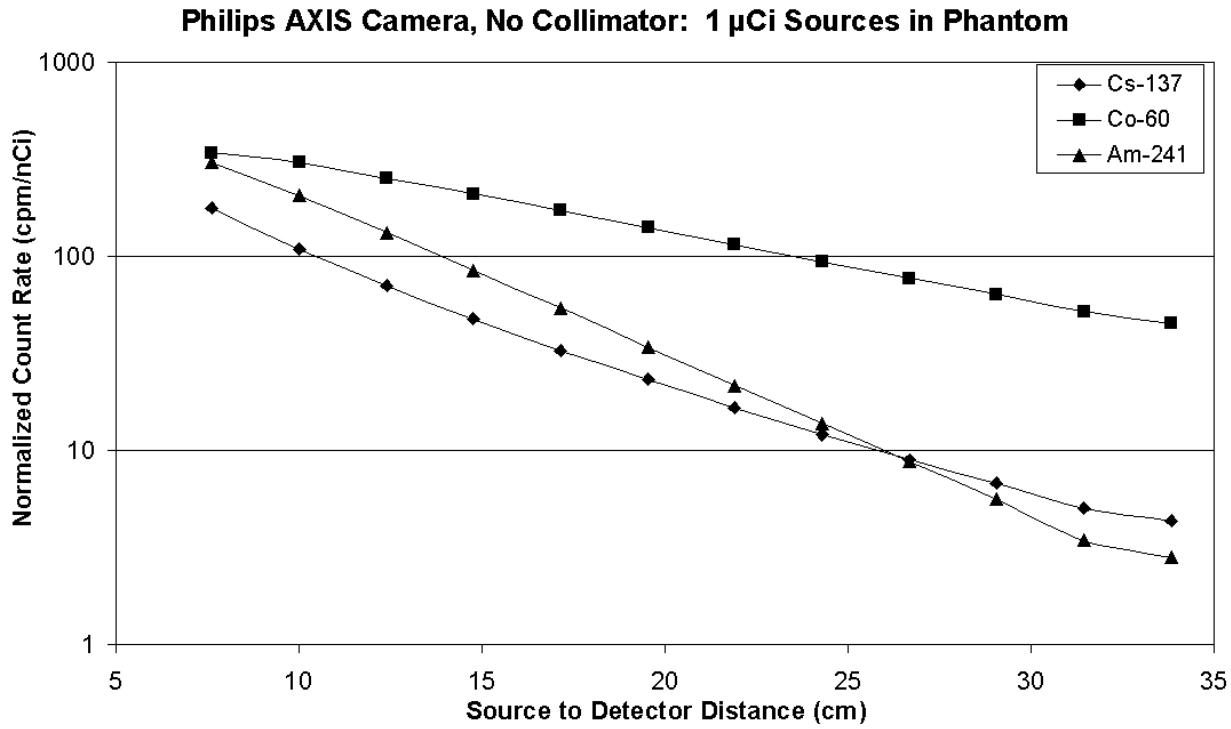

Figure 1-23. Normalized Count Rates in AXIS Camera from 1 µCi Sources in Acrylic Phantom

Next, the collimator was replaced on the camera and the set of measurements was repeated. In this experiment, the front face of the phantom was placed 8.9 cm from the face of the collimator. Since the collimator assembly is approximately 2.7 cm thick, the phantom was 11.6 cm from the detector window. As was noted earlier, a 1-µCi source of ^{241}Am cannot be reliably detected with the LEGAP collimator in place; therefore, these measurements were performed only on ^{60}Co and ^{137}Cs. The same energy windows were used as in the measurements without a collimator. The results are shown in Figure 1-24. As was observed during the in-air measurements, the collimator reduces the count rate from ^{60}Co by about a factor of 2, while the ^{137}Cs count rate is reduced about 5-fold.

The phantom studies were repeated, using the 18 µCi ^{192}Ir source. The results are displayed in Figure 1-25. The collimator produces a 6-to-8-fold reduction in the count rate.

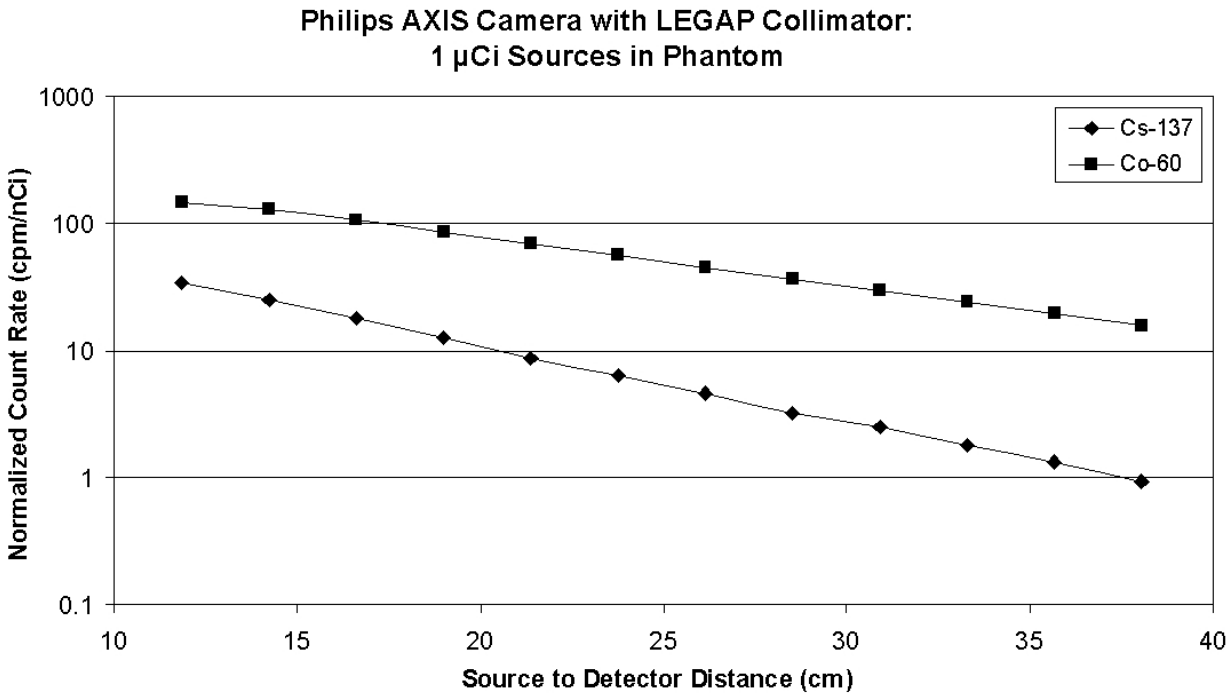

Figure 1-24. Normalized Count Rates in AXIS Camera with LEGAP collimator from 1 µCi Sources in Acrylic Phantom

1.3.2 Thyroid Uptake System

Studies similar to those performed on the gamma cameras were carried out using the Atomlab 950 Thyroid Uptake System. The count rates from the nominal 1 µCi sources of ^{60}Co, ^{137}Cs, and ^{241}Am, as well as the nominal 10 µCi ^{241}Am source and the decayed ^{192}Ir therapy seed, were measured with the sources in air at varying distances from the face of the detector. The closest approach is 15.2 cm, the depth of the collimator (see description in Section 1.2.4). Normalized count rates from the nominal 1 µCi sources as a function of distance from the detector are

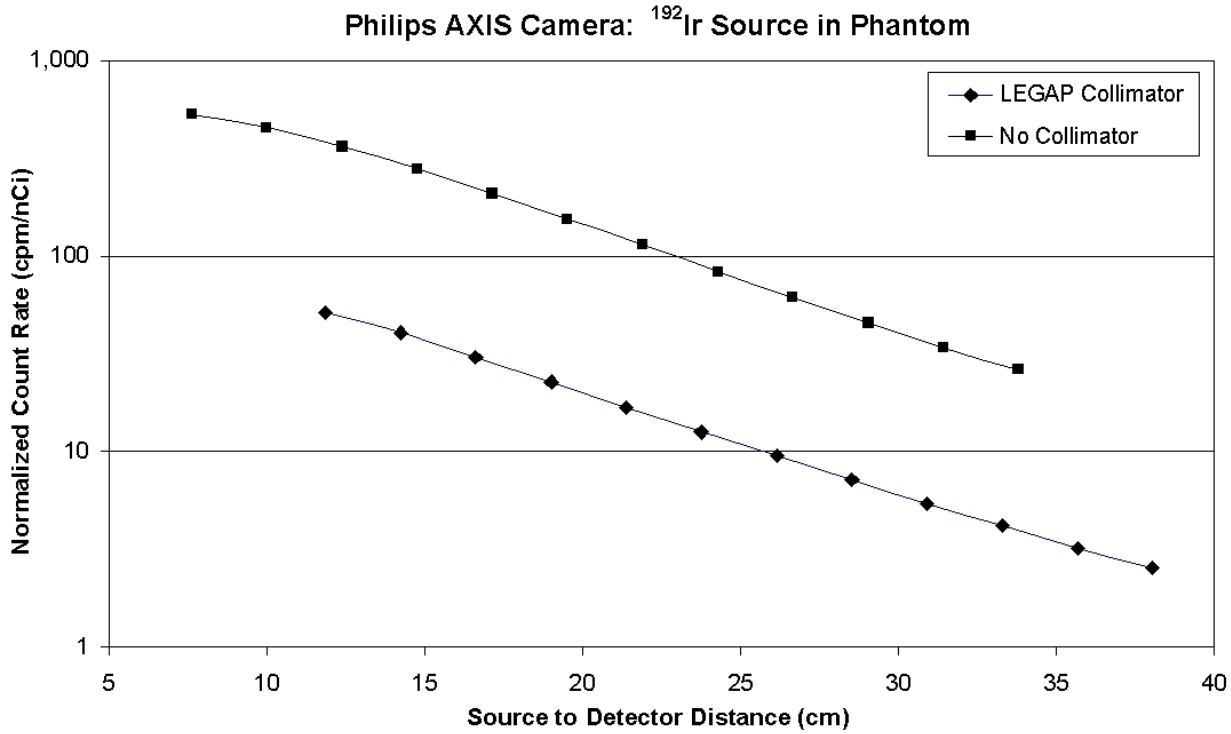

Figure 1-25. Normalized Count Rates in AXIS Camera from 18 μCi ^{192}Ir Source in Phantom

depicted in Figure 1-26,[6] while the normalized counts from the ^{192}Ir source are shown in Figure 1-27.

As can be seen in these two figures, the normalized counts from ^{192}Ir are the highest of all the five sources tested with this instrument. This is because the γ-ray spectrum of ^{192}Ir primarily falls in the range of 300 – 600 keV: the 2 × 2 inch NaI(Tl) crystal in this detector has good sensitivity to photons in this energy range. Since this radionuclide emits about 210 photons in this energy range per 100 disintegrations, a high counting efficiency would be expected. While ^{60}Co emits 200 principal γ-ray photons per 100 disintegrations, these photons have energies of either 1173 or 1332 keV. Photons of these energies are less likely to interact with the NaI(Tl) crystal; the detector is thus less efficient at counting photons of such high energies. ^{241}Am produces the third-highest counting rate. Although the 59.5 keV γ-ray photon emitted by this nuclide is efficiently captured by the NaI(Tl) crystal, the lower intensity of this radiation—36 γ-ray photons are emitted per 100 disintegrations—leads to a lower normalized count rate. The lowest normalized count rate is from ^{137}Cs. This is due to the combination of the relatively high-energy γ ray (662 keV), which is not efficiently counted by the NaI(Tl) crystal, and the fact that only 85.1 γ-ray photons are emitted per 100 disintegrations.

[6] Normalized count rates from the nominal 10 μCi ^{241}Am source, which would almost exactly overlie the 1 μCi ^{241}Am data, are not shown on this graph.

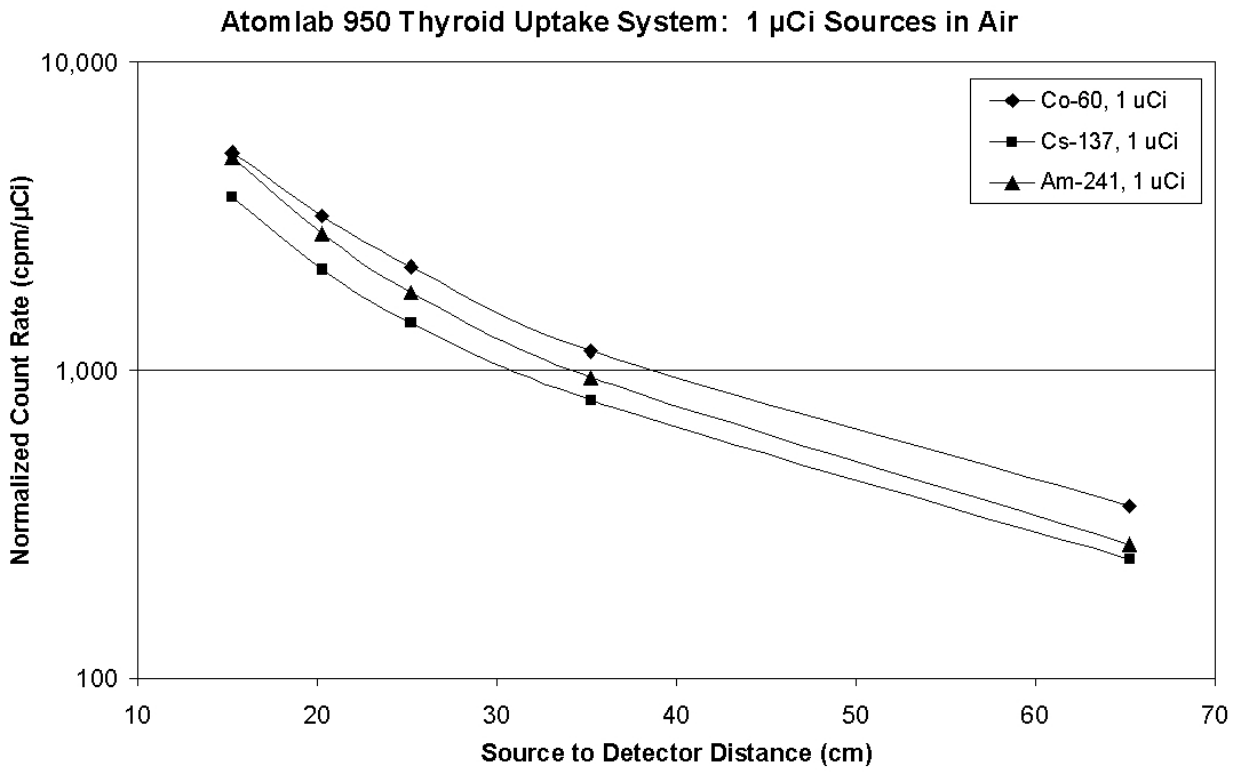

Figure 1-26. Normalized Count Rates in Atomlab 950 Thyroid Uptake System from 1 µCi Sources in Air

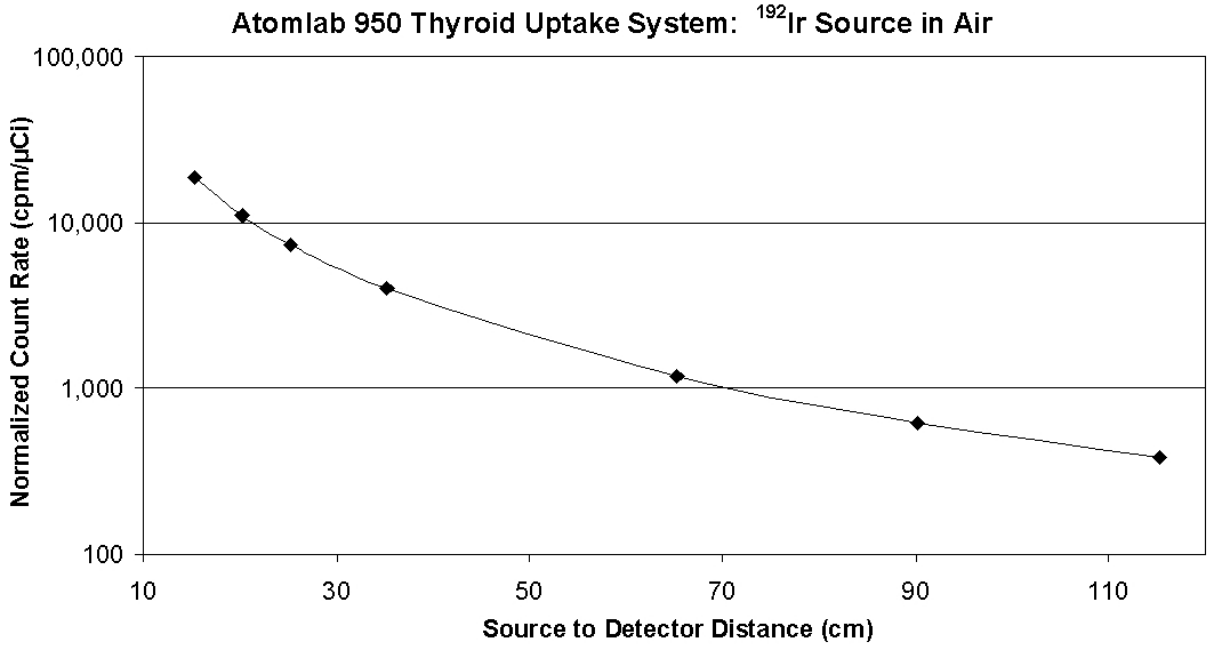

Figure 1-27. Normalized Count Rates in Atomlab 950 Thyroid Uptake System from 18 µCi ^{192}Ir Source

Further studies were performed using the acrylic slab phantom. In these tests, the face of the phantom was put in contact with the edge of the collimator, placing it 15.2 cm from the face of the detector. One-microcurie sources of ^{60}Co, ^{137}Cs, and ^{241}Am were placed at various depths within the phantom. The normalized count rates from these three sources are displayed in Figure 1-28. In this study, the ^{241}Am source produced the highest count rates up to a depth of about 2.4 cm. At greater depths, the attenuation of the low-energy γ ray reduced the count rates below those of the other two nuclides. The greater attenuation of the ^{137}Cs γ rays with respect to those from ^{60}Co can be observed in the divergence of the two curves on the semilogarithmic plot.

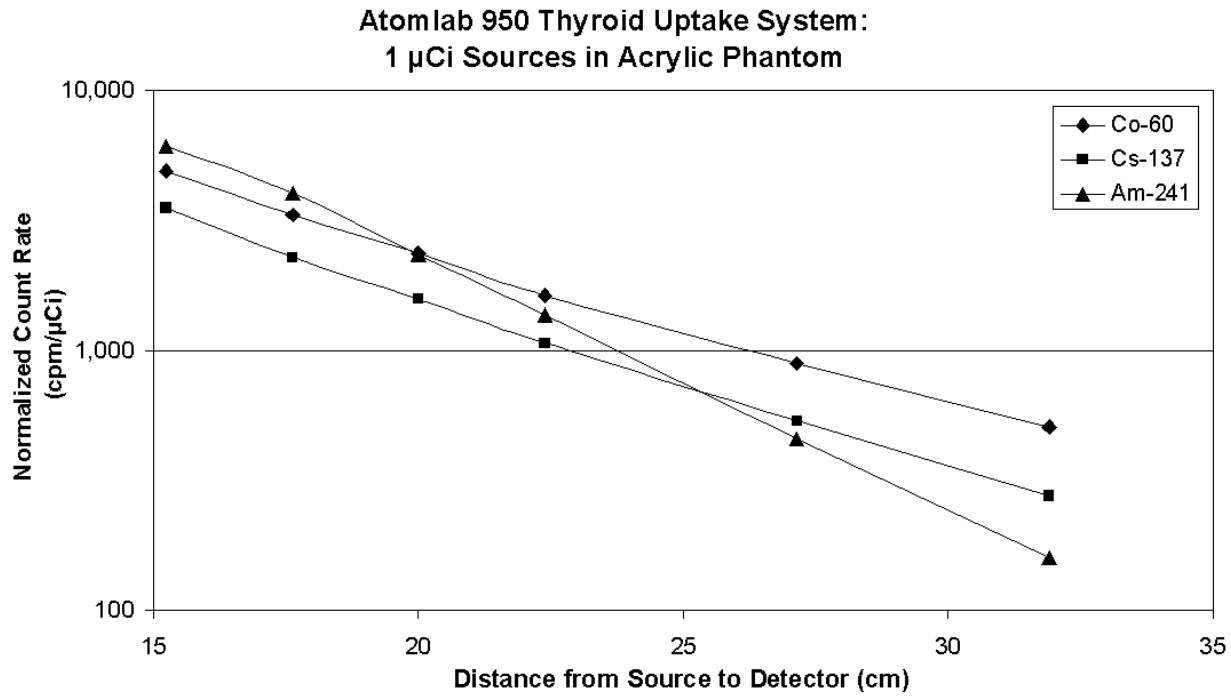

Figure 1-28. Normalized Count Rates in Atomlab 950 Thyroid Uptake System from 1 µCi Sources in Acrylic Phantom

1.3.3 Portal Monitor

As described on page 1-13, the portal monitor system consists of two NaI(Tl) detectors connected to a digital rate meter that is calibrated to display the count rate in terms of µR/h. Thus, although the interactions of γ-ray photons with NaI(Tl) detectors are registered as counts, not exposure, the count rate is translated into an exposure rate. The system is calibrated with a ^{137}Cs source: the scale on the rate meter is set to the calculated exposure rate at the location of the detector. According to information provided by the manufacturer, 1 µR/h corresponds to

1,200 cpm when the radiation source is ^{137}Cs.[7] For other photon energies, the reading is not a true exposure rate.

The exposure rates, as measured by the portal monitor, were recorded with the sealed sources at various distances from the face of the detector. Figure 1-29 shows the normalized exposure rates from the seven sealed sources. The highest rates are from ^{192}Ir, followed by ^{60}Co, as was the case for the thyroid uptake probe. However, the ^{137}Cs source produces a higher exposure rate than ^{241}Am. This difference from the thyroid probe results is attributed to the energy discrimination circuitry in the latter instrument, which is set to isolate the photopeak of each radionuclide and thus does not count the low-energy scattered radiation. Because the portal monitor employs no energy discrimination, the scattered radiation contributes to the total count rate. This low-energy scatter is a much more prominent part of the photon spectrum resulting from the interaction of the 662 keV γ ray from ^{137}Cs than of the spectrum generated by ^{241}Am, with a principal γ-ray energy of 60 keV.

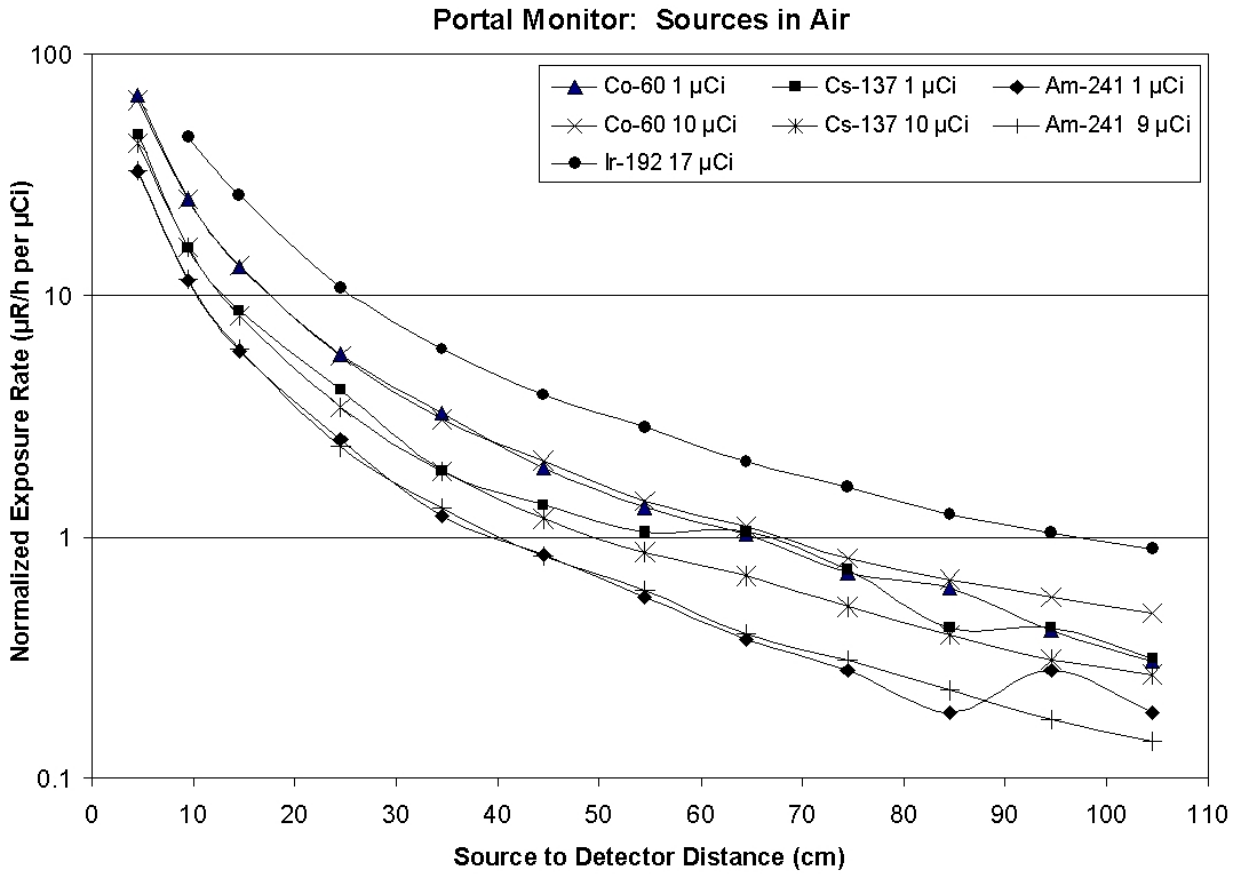

Figure 1-29. Normalized Exposure Rates Registered by Portal Monitor from Sources in Air

[7] Bill Huckabee, Ludlum Measurements, Inc., private communication with Robert Anigstein, SC&A, Inc., March 14, 2005.

The normalized exposure rates from the sources with nominal activities of 10 μCi or higher follow smooth curves out to the maximum distance of 105 cm from the detector. The *actual* recorded exposure rates from these sources are well over 1 μR/h, and are thus readily distinguishable from background, which is typically about 1.5 μR/h for this instrument in its location at HMC. For the nominal 1 μCi sources, the exposure rates begin to exhibit irregular behavior below 1 μR/h, indicating that the readings are influenced by variations in background as well as by a lack of precision in the display of the rate meter, which reads in increments of 0.1 μR/h.

The effects of attenuation by the acrylic phantom on the portal monitor readings were tested by placing the source at a fixed distance from the detector and then inserting successive slabs of the acrylic phantom between the source and the detector. In this experiment, the three nominal 10 μCi sources and the ^{192}Ir seed were held at a distance of 29.3 cm from the detector and the exposure rates were recorded as up to 10 slabs of the acrylic phantom were placed between the source and the detector. The observed exposure rates were converted to normalized count rates, using the conversion factor: 1 μR/h = 1,200 cpm. As shown in Figure 1-30, all the nuclides except ^{241}Am show an initial increase in the count rate when slabs of acrylic are placed between the source and the detector. This is attributed to the buildup of low-energy photons in the plastic as a result of the Compton scattering of the relatively high-energy primary γ rays emitted by these nuclides. This detector is more sensitive to these low-energy photons. The continuity of these curves indicates that all of these 9 to 17 μCi sources are detectable at depths of up to 24 cm in the acrylic phantom.

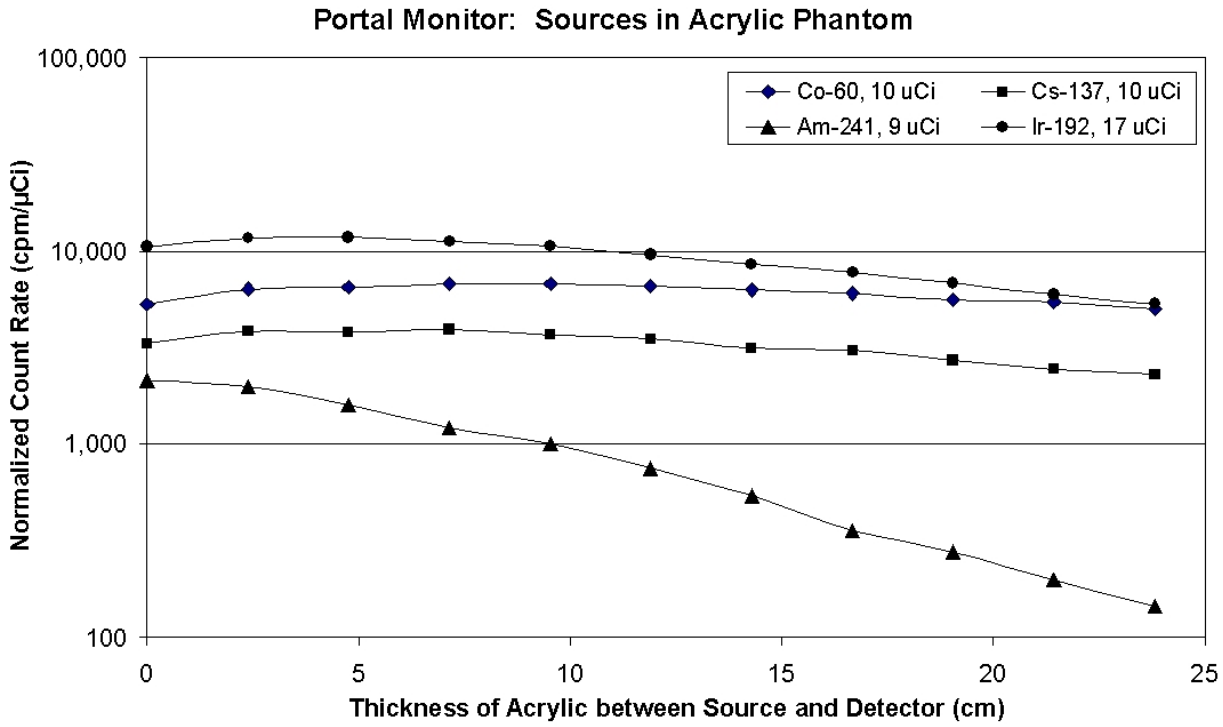

Figure 1-30. Normalized Count Rates, Converted from Portal Monitor Readings, from Sources in Acrylic Phantom

1.4 Detector Response to Discrete and Distributed ^{131}I Sources in Water-Filled Phantom

All of the measurements discussed in the foregoing sections of the report involved discrete sources, either in air or at various depths within the acrylic slab phantom. In the case of an individual internally contaminated with radioactive materials, the activity would most likely be dispersed in one or more organs. A series of experiments was performed to compare the response of each instrument to a discrete source in the center of a water-filled phantom and the response to the same activity uniformly dispersed in the water. As stated earlier, ^{131}I was chosen for this study because it is readily obtainable in aqueous solution and is commonly used in nuclear medicine. Thus, the gamma cameras and the thyroid uptake system all have preset ^{131}I energy windows, which facilitates the measurements. The phantom used for this study is described and illustrated on page 1-3 of this report.

1.4.1 Gamma Cameras

One experiment involved the Philips SKYLight camera equipped with the LEGP collimator and utilized the ^{131}I setting with a 20% energy window. The phantom with the discrete source (^{131}I in an ampule) in the center, was placed at different distances from the face of the collimator, with the broad side of the phantom facing the camera. After the ampule was broken and activity dispersed in the water, the measurements were repeated, with the phantom in the same positions as before. The results, presented in Figure 1-31, show that the count rate from the distributed source, normalized to the total activity of the source at the time of the measurement, is consistently higher (by 15% to 22%) than from the discrete source for the same position of the phantom. These results are attributed to the fact that the half-value layer of water at 364 keV (the energy of the principal γ ray of ^{131}I) is approximately 6 cm. Since the water jug is 16 cm thick, the source at the center is shielded by 8 cm of water, reducing the intensity of the γ ray by about 60%. However, for the dispersed source, the activity in the front half of the phantom undergoes much less attenuation and thus makes a disproportionate contribution to the count rate.

The experiment was repeated using the Philips AXIS camera. The results, also shown in Figure 1-31, indicate that the normalized count rate from the distributed source is consistently about 20% higher than the corresponding count rate from the discrete source. The count rates from both sources on the AXIS camera are somewhat higher than the corresponding rates on the SKYLight. This is attributed to the greater counting efficiency of the AXIS unit, which has a thicker crystal (¾-inch vs ⅜-inch in the SKYLight) and a slightly larger field of view.

1.4.2 Thyroid Uptake System

Studies were performed of the response of the thyroid uptake system to discrete and distributed ^{131}I sources in the water-filled phantom. Two different orientations of the phantom were used in these studies. In both cases, the probe was pointed in a horizontal direction. In one case, the probe was centered on the broad side of the phantom—analogous to an anterioposterior view of the body—while in the other case it was centered on the narrow side of the jug—analogous to a

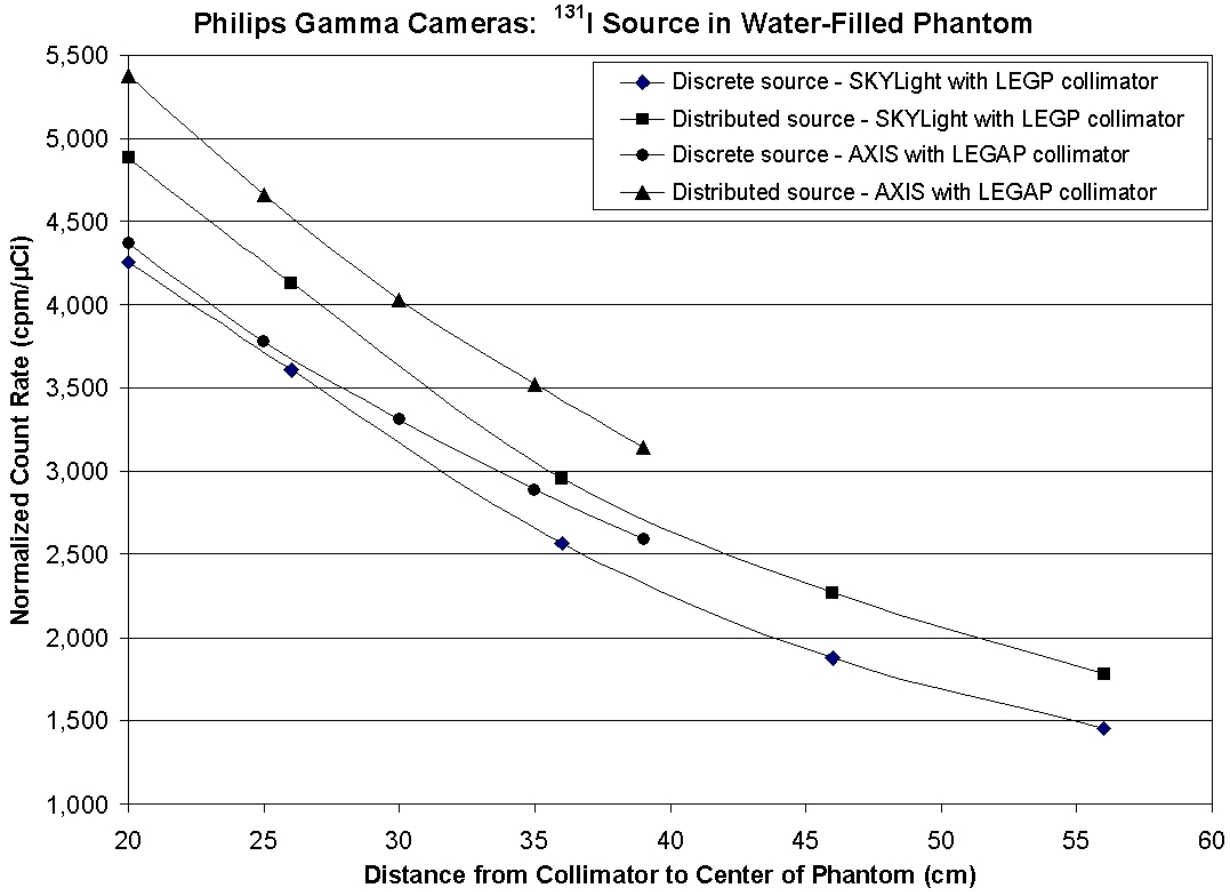

Figure 1-31. Count Rates in Philips Gamma Cameras from Discrete and Distributed ^{131}I Sources

lateral view. In both cases, count rates were measured with the phantom at varying distances from the detector, using the ^{131}I energy window built into the system.

In both orientations of the phantom the count rates from the discrete source are significantly higher than from the distributed source when the phantom is nearest to the detector, as shown in Figure 1-32. As the distance increases, the two pairs of curves approach each other: the curves cross when the center of the phantom is approximately 45 cm from the detector.

This effect is due to the narrow angle of view of the probe, as shown in the diagram in Figure 1-15. Since the probe is designed to record activity in the thyroid gland, the collimator is designed to shield out radiation from elsewhere in the body. Thus, while the discrete source at the center of the jug is always within the field of view of the detector, the source that is dispersed in the water is partially shielded by the collimator when the phantom is close to the probe. As the phantom is moved further away, more of the container comes into the field of view.

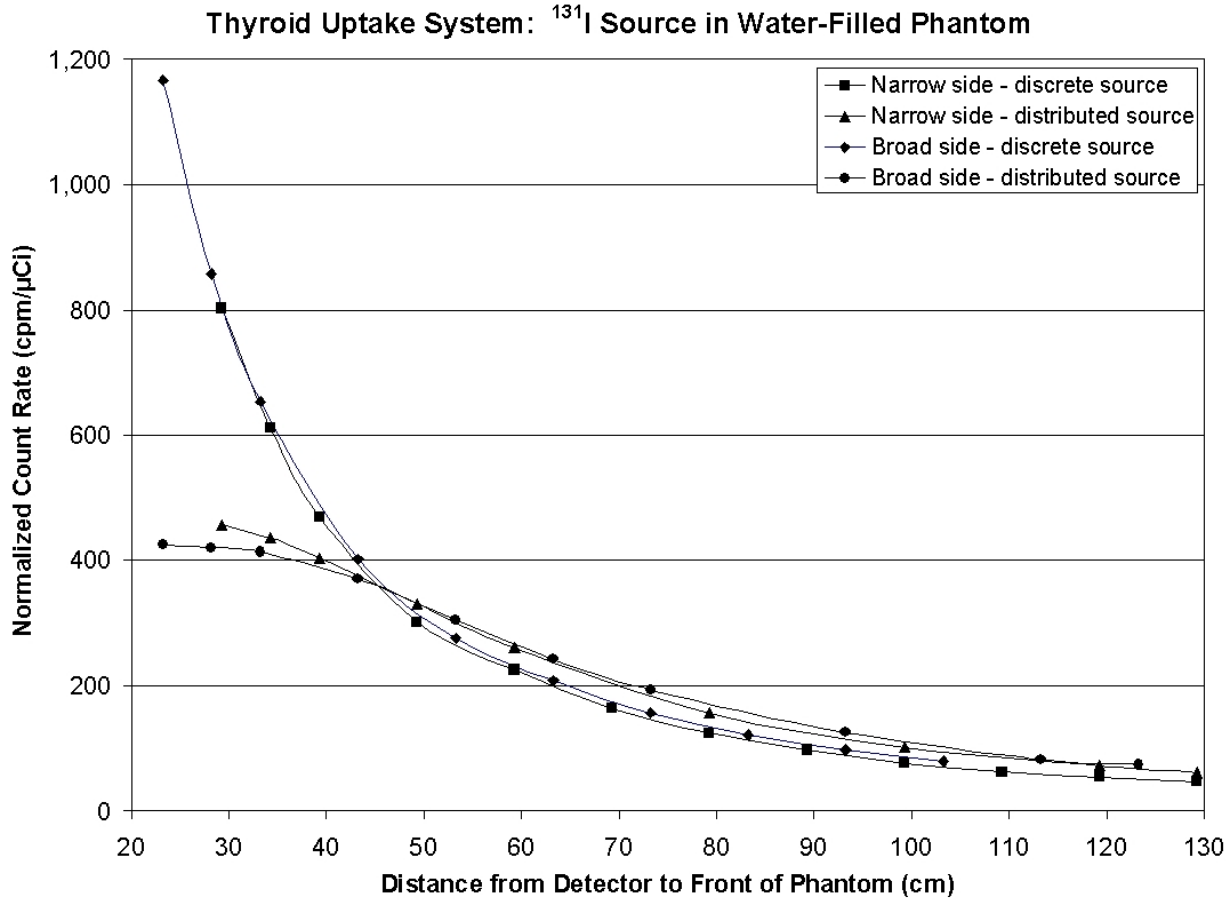

Figure 1-32. Count Rates in Atomlab 950 Thyroid Uptake System from Discrete and Distributed ^{131}I Sources

1.4.3 Portal Monitor

We compared the response of the portal monitor to discrete and distributed sources in the water-filled phantom, using a protocol similar to that employed for the thyroid uptake system. One significant difference between the portal monitor and the other instruments, as cited earlier, is the lack of pulse height discrimination in the former. Thus, scattered radiation, which is mostly rejected by the gamma cameras and the thyroid uptake system, is counted by the portal monitor. The results, presented in Figure 1-33, indicate little difference between the discrete source and the distributed source. Likewise, the recorded exposure rates show little dependence on the orientation of the phantom.

1.5 Minimum Detectable Activity (MDA)

The minimum activity that can be detected by each of the instruments discussed in the foregoing sections depends on the background count rate of a given instrument in a given configuration, the counting time, and the observed count rate, normalized to the activity of the source. The following discussion is adopted from the MARSSIM manual (NRC 2000).

Two basic quantities related to the determination of the minimum detectable activity (MDA) are the critical level and the detection limit. Assuming that the background is counted for the same period of time as the suspected radioactive source, these quantities are defined as follows:

$$L_C = k\sqrt{2B}$$

$$L_D = k^2 + 2k\sqrt{2B}$$

L_C = critical level (counts)

L_D = detection level (counts)

k = Poisson probability sum for Type I and Type II errors

B = total background counts during counting period

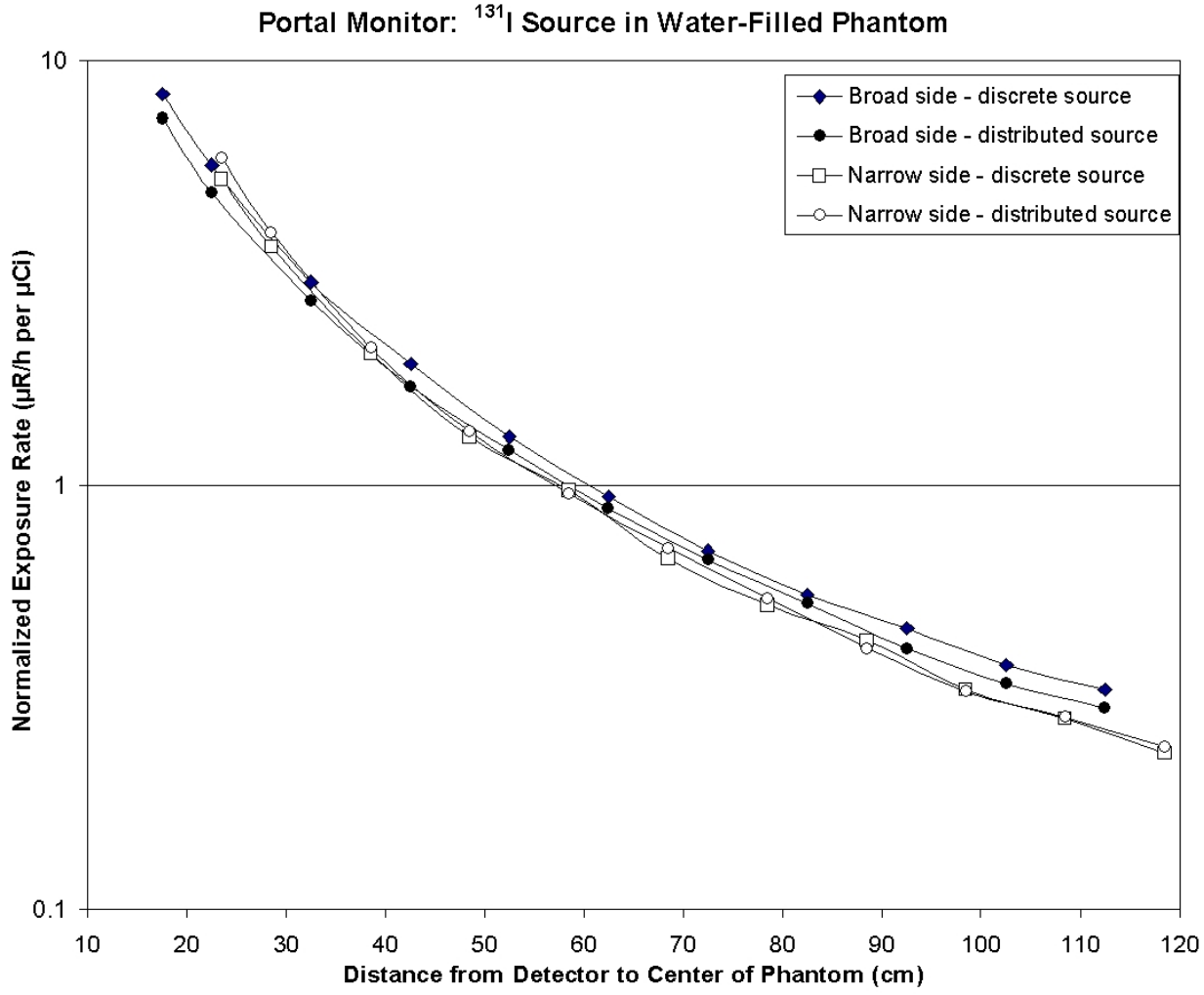

Figure 1-33. Exposure Rates on Portal Monitor from Discrete and Distributed ^{131}I Sources

A Type I error ("false positive") occurs when a detector response is considered to be above background when, in fact, only background radiation is present. A Type II error ("false negative") occurs when a detector response is considered background when, in fact, radiation is present at levels above background. If values of .05 are considered acceptable for both Type I and Type II errors, then k = 1.645.

The previous equation is then written as

$$L_C = 2.33\sqrt{B}$$

$$L_D = 3 + 4.65\sqrt{B}$$

Note: NRC 2000 recommends evaluating k^2 as 3, based on Brodsky 1992.

Although any counts above the critical level are indicative of suspected radioactive contamination, only levels above the detection limit can be used to quantify the activity of any radioactive contaminants. In actual practice, the MDA is the product of the detection limit and the normalized count rate of a given detector, in a given configuration, exposed to a given radionuclide:

$$A_{ijk} = \frac{3 + 4.65\sqrt{\frac{b_{jk}}{t_c}}}{n_{ijk}} \qquad (1\text{-}1)$$

A_{ijk} = minimum activity of radionuclide *i* detectable by detector *j* in configuration *k*

n_{ijk} = normalized count rate of detector *j* in configuration *k* exposed to radionuclide *i*

b_{jk} = background count rate of detector *j* in configuration *k* (cpm)

t_c = counting time for both background and suspected radioactive source (min)

Note: "configuration" refers to both the settings of the detector system (i.e., peak energy and width of energy window) and the source geometry (e.g., distance, thickness of phantom).

1.5.1 Phantom Studies

Preliminary MDAs were calculated for representative configurations of each detector system and each radionuclide, according to Equation 1-1. The calculations were for a discrete source at selected depths within the acrylic phantom that correspond to activity in the lungs. The appropriate locations within the acrylic phantom were selected by comparing this phantom to the phantoms (mathematical models of Reference Man) that are used to calculate radiation transport in the human body.

In the mathematical phantom of a 21-year-old male, based on the description by Cristy and Eckerman (1987) that is used in the analysis presented in Chapter 2, the chest wall has a thickness of 2.1 cm and an average density of 1.04 g/cm^3, resulting in a mass thickness of 2.18 g/cm^2. This is comparable to one slab of the acrylic phantom, which has a nominal thickness of 2.38 cm and a density of 1.19 g/cm^2, resulting in a mass thickness of 2.83 g/cm^2. The maximum dimension in the anterioposterior direction (i.e., front to back) of the lung cavity in the Cristy phantom is 14.4 cm. The lung region of this model has a density of 0.296 g/cm^3, yielding a mass thickness of 4.26 g/cm^2. Thus, the total mass thickness from the front of the chest to the rear of the lung cavity is 6.45 g/cm^2. This falls between the mass thickness of two slabs of acrylic—5.67 g/cm^2—and that of three slabs—8.50 g/cm^2. Therefore, sources at depths of 2.4, 4.8, and 7.1 cm, corresponding to one, two, and three slabs of the acrylic phantom, were selected to represent the response of detector systems to radionuclides in the lungs. Although, strictly speaking, the acrylic phantom is not tissue-equivalent in terms of its elemental composition, the attenuation of γ rays from ^{60}Co, ^{137}Cs, and ^{192}Ir is primarily due to Compton scattering and is thus not strongly affected by the exact composition of the material. The acrylic phantom is a less precise surrogate for human tissue for the lower-energy ^{241}Am emissions.

Gamma Camera

The normalized count rates recorded by the AXIS camera, with and without a collimator, from sources at three different depths in the acrylic phantom, are listed in Table 1-4, along with MDAs corresponding to counting times of 1 – 10 minutes. In all cases, use of the camera without a collimator would produce lower MDAs. The annual limits on intake (ALIs) for occupational exposure via inhalation, based on the most restrictive chemical form (Eckerman et al. 1988), are listed for reference. As shown in this table, the MDAs for the three β-γ emitters—^{60}Co, ^{137}Cs and ^{192}Ir—are three to five orders of magnitude below the ALIs. The MDAs for ^{241}Am are comparable to the ALIs.

Several cautions should be noted in drawing conclusions from such a comparison. One is that the MDAs of activities distributed in the lungs, assessed by the AXIS camera utilizing the optimized energy windows described in Section 2.4.1, would be lower than those shown in Table 1-4, due to the greater sensitivities afforded by these energy windows. However, since background count rates corresponding to such windows have not been measured, these MDAs could not be quantitatively estimated at the present time. A further discussion of the significance of the calculated MDAs for the exposure assessment is presented in Section 1.7.

Thyroid Uptake System

The corresponding data for the thyroid uptake system are listed in Table 1-5. The MDAs are higher than those calculated for the AXIS camera without a collimator for all four radionuclides. They are also higher than those for the AXIS camera with a collimator for all nuclides except ^{241}Am: as noted earlier, microcurie sources of this nuclide could not be reliably counted on the AXIS system with the collimator in place. As was the case for the AXIS camera, the MDAs for the three β-γ emitters are orders of magnitude below the ALIs. The MDAs for ^{241}Am are comparable to the ALIs, depending on the depth of the source in the phantom and the counting time.

Table 1-4. Normalized Count Rates for AXIS Camera and MDAs Using Various Counting Times for Sources in Acrylic Phantom

	Nuclide	ALI[a] (nCi)	Background (cpm)	Depth (cm)	Count rate (cpm/nCi)	Counting time (min) 1	2	3	5	10
						MDA (nCi)				
No Collimator	Co-60[b]	30,000	18,200	2.4	303.6	2.1	1.5	1.2	0.9	0.7
				4.8	253.0	2.5	1.8	1.4	1.1	0.8
				7.1	211.3	3.0	2.1	1.7	1.3	1.0
	Cs-137[c]	200,000	2,200	2.4	108.7	2.0	1.4	1.2	0.9	0.7
				4.8	70.7	3.1	2.2	1.8	1.4	1.0
				7.1	47.6	4.6	3.3	2.7	2.1	1.5
	Ir-192[d]	20,000	22,000	2.4	454.0	1.5	1.1	0.9	0.7	0.5
				4.8	361.2	1.9	1.4	1.1	0.9	0.6
				7.1	277.8	2.5	1.8	1.4	1.1	0.8
	Am-241[e]	6	26,700	2.4	206.6	3.7	2.6	2.1	1.7	1.2
				4.8	131.4	5.8	4.1	3.4	2.6	1.9
				7.1	84.5	9.0	6.4	5.2	4.1	2.9
LEGAP Collimator	Co-60[b]	30,000	9,300	2.4	129.7	3.5	2.5	2.0	1.6	1.1
				4.8	106.3	4.2	3.0	2.5	1.9	1.4
				7.1	85.9	5.3	3.7	3.0	2.4	1.7
	Cs-137[c]	200,000	1,600	2.4	25.2	7.5	5.3	4.4	3.4	2.5
				4.8	17.9	10.6	7.5	6.2	4.8	3.5
				7.1	12.6	15.0	10.7	8.8	6.8	4.9
	Ir-192[d]	20,000	9,522	2.4	40.6	11.3	8.0	6.5	5.1	3.6
				4.8	30.3	15.1	10.7	8.7	6.8	4.8
				7.1	22.6	20.2	14.3	11.7	9.1	6.5

[a] Annual limits on intake for occupational exposure via inhalation, based on most restrictive chemical form (Eckerman et al. 1988)

[b] 1 µCi source counted in 100% ^{137}Cs energy window

[c] 1 µCi source counted in 20% ^{137}Cs energy window

[d] 18 µCi source counted in 100% ^{18}F energy window

[e] 1 µCi source counted in 100% ^{133}Xe energy window

Portal Monitor

As is discussed on page 1-25, the exposure rates recorded by the portal monitor were converted to count rates. To calculate the MDAs, we also need to estimate the effective counting time for this instrument. Steinmeyer (1998) states that the effective counting time for a detector connected to a rate meter is twice the time constant of the rate meter. However, the specifications for the rate meter on the Ludlum waste monitor cite the response time rather than the time constant. According to a Ludlum report cited by Steinmeyer, the time constant is equal to approximately 44% of the response time. Thus, since the response time of the rate meter on the portal monitor is 3 seconds, as stated on page 1-14 of the present report, the effective counting time is 2.64 s ($2 \times .44 \times 3 = 2.64$). The normalized count rates and the calculated

MDAs for the portal monitor system are shown in Table 1-6. As would be expected for an instrument that has a high background count rate relative to its counting efficiency and a short effective counting time, the MDAs are one to two orders of magnitude higher than those for the gamma camera or the thyroid uptake system. Again, the MDAs for the three β-γ emitters are orders of magnitude below the ALIs; however, for ^{241}Am, they are two orders of magnitude greater than the ALI. This instrument can play a useful role in screening individuals for internal radioactive contamination with high-energy γ emitters.

Table 1-5. Normalized Count Rates for Atomlab 950 Thyroid Uptake System and MDAs Using Various Counting Times for Sources in Acrylic Phantom

Nuclide	ALI (nCi)	Background (cpm)	Depth (cm)	Count rate (cpm/nCi)	Counting time (min)				
					1	2	3	5	10
					MDA (nCi)				
Co-60	30,000	56	2.4	3.31	11.4	8.3	7.0	5.6	4.2
			4.8	2.37	15.9	11.6	9.7	7.8	5.9
			7.1	1.63	23.1	16.9	14.1	11.4	8.6
Cs-137	200,000	62	2.4	2.28	17.4	12.7	10.6	8.5	6.4
			4.8	1.58	25.0	18.2	15.2	12.2	9.2
			7.1	1.07	37.0	27.0	22.6	18.1	13.6
Ir-192	20,000	186	2.4	12.27	5.4	3.9	3.2	2.6	1.9
			4.8	8.22	8.1	5.8	4.8	3.8	2.8
			7.1	5.62	11.8	8.5	7.1	5.6	4.1
Am-241	6	34	2.4	4.02	7.5	5.5	4.6	3.8	2.9
			4.8	2.33	12.9	9.5	8.0	6.5	5.0
			7.1	1.37	21.9	16.1	13.6	11.0	8.4

1.6 Provisional Calibration Factors

The normalized count rates presented in Tables 1-4/1-6 could, in principle, be used to derive calibration factors for the use of the three instruments in assessing the activities of radioactive materials in the lungs of exposed individuals. In the case of the Philips AXIS camera, these data are superceded by calibration factors derived from computer analyses utilizing Monte Carlo simulations, as discussed in Section 1.6.1.

Pending more definitive analyses of the thyroid uptake system and the portal monitor, the count rates in Tables 1-5 and 1-6, respectively, can be used as the bases of provisional calibration factors for these two instruments. The most useful values are those for sources attenuated by two slabs of the acrylic phantom—i.e., sources at a depth of 4.8 cm. This location most closely approximates a source near the center of the lung.

1.6.1 Gamma Camera

Chapter 2 of the present report describes the derivation of calibration factors for two models of the AXIS camera—one equipped with a ¾-inch crystal, the other with a ⅜-inch crystal, both

used without a collimator—utilizing energy windows optimized for enhanced sensitivity. These recommended calibration factors are listed in Table 2-3. These factors were derived by Monte Carlo simulations based on a realistic model of an anthropomorphic phantom of an adult male, mathematical models of the AXIS cameras based on detailed design drawings and specifications, current radioactive decay data, and an accurate radiation transport model. The methodology used in the computer analyses was validated by comparing predicted count rates with the results of measurements on the AXIS camera with a ¾-inch crystal that are presented in the present chapter.

Table 1-6. Normalized Exposure Rates and MDAs for Portal Monitor System: Sources in Acrylic Phantom

Nuclide	ALI (nCi)	Background[a] (cpm)	Depth (cm)	Exposure rate (μR/h per μCi)	Count rate[a] (cpm/nCi)	MDA (nCi)
Co-60	30,000	1,680	2.4	5.3	6.4	143
			4.8	5.4	6.5	140
			7.1	5.6	6.7	136
Cs-137	200,000		2.4	3.2	3.8	238
			4.8	3.2	3.8	240
			7.1	3.3	3.9	233
Ir-192	20,000		2.4	9.7	11.7	78
			4.8	9.8	11.8	77
			7.1	9.3	11.2	82
Am-241	6		2.4	1.6	2.0	461
			4.8	1.3	1.6	571
			7.1	1.0	1.2	752

Note: Effective counting time: 2.64 s

[a] Calculated from observed exposure rate

These calibration factors, along with the recommended window settings, should be employed in the event that one of the Philips AXIS cameras were used to assess the activity in the lungs of an individual who had inhaled dispersed airborne activities of one of the four radionuclides. The use of a camera with a collimator is not recommended for this purpose. First, the sensitivity of detection is significantly reduced by the collimator. Second, reliable calibration factors could not be derived due to the difficulty of reliably modeling the collimator.

1.6.2 Thyroid Uptake System

The normalized count rates listed in Table 1-5 can serve as the bases for provisional calibration factors for the thyroid uptake system, provided appropriate adjustments are made for the geometry of the source and the detector. As shown in Figure 1-15, the detector has a narrow angle of view that would not encompass the entire chest unless the exposed individual was placed at some distance from the probe. This effect is demonstrated by the data on the water-filled phantom, which are presented on page 1-28. Therefore, the count rates from a discrete

source that is 4.8 cm from the edge of the conical collimator, the position of the source in the acrylic phantom, are an overestimate of the count rates from a source distributed in the lungs.

To approximate the response of the detector to activity distributed throughout the lungs, we must first correct for the distance of the centroid of the activity from the front of the detector. Since the collimator provides a 15.2-cm standoff, and since the center of the chest is assumed to be 9.3 cm from the front surface, the total distance is 24.5 cm. However, the source in the acrylic phantom is only 20 cm from the detector. We can correct for this difference by comparing the count rates from sources in air 20.2 and 25.2 cm from the detector, the distances included in the data shown in Figures 1-26 and 1-27 that are nearest to the desired distances. The average ratio of the count rates at these two distance from the four radionuclides is 1.50. Next, we estimate the count rates from the discrete ^{131}I source in the water-filled phantom at a distance of 24.5 cm from the detector by interpolating between the count rates at adjacent distances, using the data collected with the broad side of the jug facing the detector which are displayed in Figure 1-28. We then estimate the count rate at the same distance from the same source dispersed in the phantom. The ratio of these interpolated count rates is equal to 1.78. We then multiply this factor by 1.50, the correction factor for the distance, and obtain an overall correction factor of 2.68. If we divide the observed count rates from sources at a depth of 4.8 cm in the acrylic phantom by this factor, we obtain approximate calibration factors for the four radionuclides distributed in the lungs. In actual practice, the count rates will be more variable than those obtained with the gamma camera. In the latter case, because of the large angle of view, the count rates are less sensitive to variations in the exact position of the exposed individual and to variations in body dimensions.

Provisional calibration factors for this instrument are summarized in Table 1-7.

Table 1-7. Provisional Calibration Factors

Nuclide	Thyroid Uptake System[a] (cpm/μCi)	Portal Monitor (μR/h per μCi)
Co-60	884	5.4
Cs-137	591	3.2
Ir-192	3,067	9.8
Am-241	870	1.3

[a] Calibration factors were reduced by a factor of 2.68 to compensate for the exposure geometry (see text).

1.6.3 Portal Monitor

In the case of the portal monitor, the source in the acrylic phantom was about 29 cm from the detector. The detector is shielded by a protective acrylic panel whose front surface is 4.5 cm from the face of the detector; therefore, in an individual whose chest is pressed against the acrylic panel, the center of the chest would be about 14 cm from the detector. Data from the study on the water-filled phantom indicates that the count rates from the discrete source are

about 15% higher than from the same source dispersed in the phantom. Based on these observations, we can conclude that the calibration data for the portal monitor would enable reasonably conservative estimates of activity in the lungs of an exposed individual, the lowered count rate from the activity distributed in the chest being compensated by a closer distance to the detector. These results show that the portal monitor, if closely watched by a trained observer, is a useful screening tool for inhaled activities of any of the three β-γ emitters addressed in this study. Provisional calibration factors are listed in Table 1-7.

1.6.4 Application of Results

Of the three instruments on which definitive measurements were performed, the ¾-inch AXIS camera without a collimator, along with a similar camera with a ⅜-inch crystal that was included in the Monte Carlo simulations reported in Chapter 2, are by far the preferred systems for assessing individuals with radioactive material that is deposited in the lungs. However, the calibration factors for these instruments that are listed in Table 2-3 apply only to the four radionuclides addressed by the present study, and only to the energy windows for each radionuclide that are listed in that table.

1.7 Conclusions

These preliminary studies of representative instruments commonly found in hospitals show that such instruments can play a useful role in the screening and assessment of individuals who have inhaled airborne radioactive materials. The three β-γ emitters can be detected by any of these instruments at levels of activity in the lungs that are a small fraction of the ALI. This is not so in the case of ^{241}Am, which has much higher MDAs than the other nuclides, coupled with a much lower ALI. Only a gamma camera without a collimator, operated under optimum conditions, is appropriate for screening individuals potentially exposed to inhalation of this radionuclide.

The estimate of activity in the lungs at the time of the assessment is but the first step in determining the intake of a given radionuclide or the prospective dose. It is also necessary to estimate the fraction of the inhaled activity that is present in the lungs at the time of the assessment. Information useful in performing such estimates can be found in several recent publications. ICRP Publication 66 (ICRP 1994) presents a revised kinetic and dosimetric model of the human respiratory tract. The "Hanford Internal Dosimetry Technical Basis Manual" (PNNL 2004) lists procedures for determining the body burdens of radioisotopes of various elements, including cobalt, strontium, cesium, plutonium, and americium. This list encompasses three of the elements included in the present study: biokinetic data for iridium is found in ICRP Publication 30, part 2 (ICRP 1980). Finally, the National Council on Radiation Protection and Measurements (NCRP) is currently preparing a report, to be entitled "Management of Persons Contaminated with Radionuclides," that addresses these issues.

Similar caution is needed in comparing the MDA or any estimated activities in the lung, using the experimental results presented in this chapter, to the ALI. Since the ALI refers to intake, not to the activity present in the lungs at any given time, these comparisons may useful for screening purposes but do not, by themselves, form a basis for a clinical assessment.

Finally, the calibration factors are based on the assumption that only the activities in the lungs contribute to the count rates registered in these instruments. If some of the activity has migrated to other organs and tissues, such activities may contribute to the count rates, leading to an elevated estimate of the activity in the lungs.

References

Amersham Health. 2004. *The Encyclopaedia of Medical Imaging.* Vol. 1. <http://www.amershamhealth.com/medcyclopaedia/printout.asp?url=Volume%20I/ANGER%20CAMERA.html> (March 29, 2005)

Brodsky, A. 1992. "Exact Calculation of Probabilities of False Positives and False Negatives for Low Background Counting." *Health Physics, 63*(2), 198-204.

Cristy, M., and K. F. Eckerman. 1987. "Specific Absorbed Fractions of Energy at Various Ages from Internal Photon Sources. I. Methods," ORNL/TM-8381/V1. Oak Ridge, TN: Oak Ridge National Laboratory.

Eckerman, K. F., A. B. Wolbarst, and A. C. B. Richardson. 1988. "Limiting Values of Radionuclide Intake and Air Concentration and Dose Conversion Factors for Inhalation, Submersion, and Ingestion," Federal Guidance Report No. 11, EPA-520/1-88-020. Washington, DC: U.S. Environmental Protection Agency, Office of Radiation Programs.

International Commission on Radiological Protection (ICRP). 1980. "Limits for Intakes of Radionuclides by Workers," ICRP Publication 30, Part 2. *Annals of the ICRP, 4*(3-4). Oxford: Pergamon Press.

International Commission on Radiological Protection (ICRP). 1994. "Human Respiratory Tract Model for Radiological Protection," ICRP Publication 66. *Annals of the ICRP*, *24*(1-3), Oxford: Pergamon Press.

Isotope Products Laboratories (IPL) 2003. "Reference & Calibration Sources." <http://www.ipl.isotopeproducts.com/new_ipl_site/pdf/Std_Cat03.pdf> (March 29, 2005).

Marconi Medical Systems, Inc. 2001. "AXIS/IRIX Operator Guide," T55B-1465.D. Author.

North American Scientific (NAS). 2005. "Gamma Source Calibration." <http://www.nomos.com/page?id=1481> (February 4, 2005).

Nuclear Regulatory Commission (U.S.) (NRC). 2000. "Multi-Agency Radiation Survey and Site Investigation Manual (MARSSIM)," NUREG-1575, Rev. 1. Washington, DC: Author.

Pacific Northwest National Laboratory, Environment, Safety, and Health Systems (PNNL). 2004. "Hanford Internal Dosimetry Technical Basis Manual," PNNL-MA-860. <http://www.pnl.gov/eshs/pub/pnnl860.html> (October 14, 2005).

Steinmeyer, P., Jr. 1998. "Detection Sensitivity and MDA (Part 1)." *Ludlum Report, 13*(1) 2-3. <http://www.ludlums.com/ReNwsLtr/NwsLtr-42re.pdf> (March 29, 2005).

Chapter 2

MONTE CARLO SIMULATIONS OF COUNT RATES IN GAMMA CAMERAS

Chapter 1 of the present report describes the measurement of count rates from radioactive sources on several radiation detection and imaging instruments commonly used in hospitals and other medical facilities. These count rates were measured with discrete sources of four different radionuclides in air. Additional measurements were performed with these sources at different positions within a phantom constructed of acrylic slabs. This phantom was intended to yield a rough approximation of the attenuation and scatter of radioactive contaminants inside the human body. The measured count rates from sources within the acrylic phantom were used to derive a set of provisional calibration factors for each of four radionuclides using two different instruments.

The present chapter describes the use of Monte Carlo computer models to calculate count rates in two models of gamma cameras from radionuclides uniformly distributed in the lungs. These calculations form the basis for calibration factors for the use of these instruments in assessing activities in the lungs of exposed individuals.

2.1 Methodology

2.1.1 Computer Models

The calculations necessitated the construction of mathematical models of two gamma cameras. They also required a mathematical model of the human body, and a model to simulate the transport of photon radiation from the radioactive sources to the detector and the interaction of these photons with the detector. We will begin by describing the radiation transport model used in these calculations.

Radiation Transport Model

Radiation transport was modeled by means of the Los Alamos Monte Carlo code MCNP5 (LANL 2004a). LANL 2004b presents the following description of this code:

> MCNP is a general-purpose Monte Carlo N-Particle code that can be used for neutron, photon, electron, or coupled neutron/photon/electron transport . . . . The code treats an arbitrary three-dimensional configuration of materials in geometric cells bounded by first- and second-degree surfaces and fourth-degree elliptical tori.
>
> Pointwise cross-section data are used. . . . For photons, the code accounts for incoherent and coherent scattering, the possibility of fluorescent emission after photoelectric absorption, absorption in pair production with local emission of annihilation radiation, and bremsstrahlung. . . . Important standard features that make MCNP very versatile and easy to use include a powerful general source . . . both geometry and output tally plotters; a rich collection of variance reduction techniques; a flexible tally structure; and an extensive collection of cross-section data. . . .

MCNP5 is the latest version of this code. An earlier version was one of the radiation transport codes used to calculate the dose conversion coefficients presented in ICRP Publication 74 (ICRP 1996). ICRP found good agreement among the several different codes used for this publication, which constitutes a benchmark and helps justify the use of MCNP5 for the present analysis. Los Alamos National Laboratory has also conducted extensive benchmarking studies of this code.

The present analysis utilized the MCNPLIB04 photon cross-section library, which was released in 2002 and is the latest release to date. This library is based on the Evaluated Nuclear Structure Data File (ENSDF) maintained by the Brookhaven National Laboratory. All simulations were performed without explicit electron transport. Secondary electrons were assumed to deposit their energy locally—an appropriate assumption for the large detectors in the gamma cameras.

Models of Gamma Cameras

The Philips gamma cameras used in the present study are described in Section 1.2.3 of the present report. A schematic diagram of the internal construction of a typical gamma camera is shown in Figure 2-1. Additional components include a heavy lead shield that surrounds the crystal and the photomultiplier tubes (PMTs).

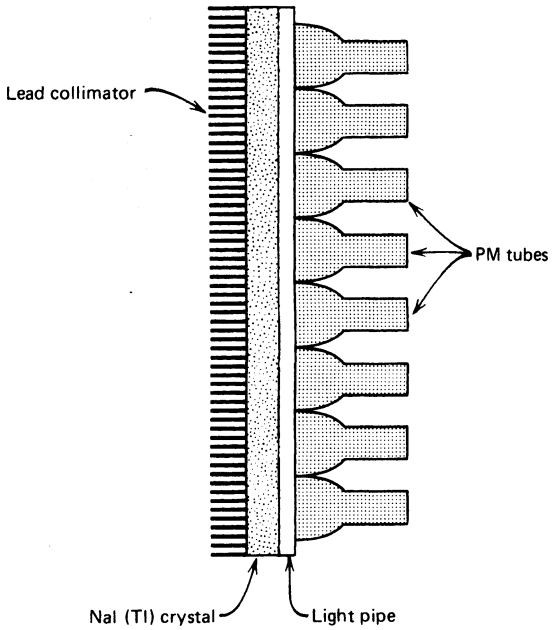

Figure 2-1. Key Components of Gamma Camera (Knoll 2000)

The Philips AXIS gamma cameras were represented by mathematical models that described details of their mechanical construction, including the geometrical dimensions, density, and composition of the major components. Sufficient detail was included to enable the accurate simulation of the interaction of the ionizing photon radiation emitted by the radioactive sources with the detector, including energy deposition in the crystal and attenuation and scattering by various components.[8]

The following description of the model of the detector head of the AXIS camera is taken from Staelens et al. (2003):

> Figure 2-2 shows a detailed model of the detector head geometry starting from the collimator and incorporating the crystal in its casing before the light guide, the PMTs and the compression plate, further on to the air gap, the lead ending and the shielding. Different

[8] The authors wish to acknowledge the assistance of Philips Medical Systems, N. A. in providing the design specifications and other data that enabled us to construct realistic models of the AXIS cameras. Our special thanks go to Jody L. Garrard, Nuclear Medicine Product Manager; Mike Petrillo, Principal Engineer, SPECT Detector Engineering; and John Vesel, all of whom gave generously of their time and effort in support of this project.

materials (aluminium, [borosilicate][9] glass, NaI, lead, plastic), linked to their cross sections for photon interaction, were specified in order to provide a realistic model for the AXIS detector head.

The detector head model was thus composed of an aluminium cover around the NaI crystal . . . . A light guide made of thick [borosilicate] glass was positioned behind the embedded crystal, followed by the PMTs, modeled as [borosilicate glass filling the volume encased by the mu-metal shields. The glass was modeled as a diffuse mass—the total mass matched the actual mass of the PMTs.] The back compartment of the detector was ended by an aluminium compression plate, an air gap and a lead shielding covering all [five] sides of the detector.

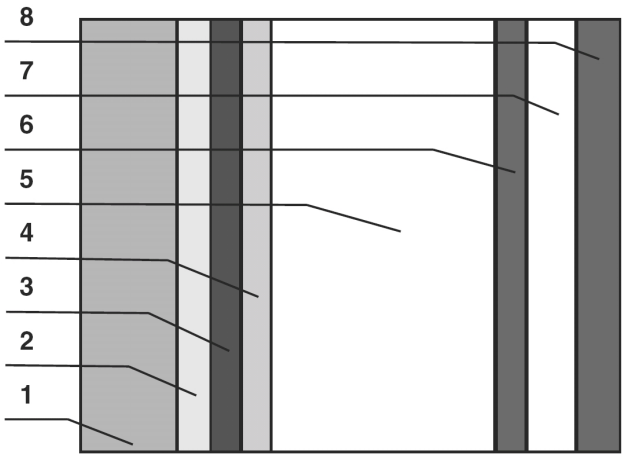

Figure 2-2. Axial view of the detector head model with 1: collimator, 2: cover, 3: crystal in its aluminium casing, 4: light guide, 5: PMTs, 6: compression plate, 7: air gap and 8: lead shield (top and bottom shielding of the crystal is omitted for visualization purposes) (Staelens et al. 2003)

Model of the Human Body

The human body was represented by a mathematical phantom generated by BodyBuilder, a commercial computer program from White Rock Science. As described by Van Riper (2004):

The human models produced by BodyBuilder are based on the descriptions for several ages (newborn, ages 1, 5, 10, and 15 years, adult female, and adult male) given in an Oak Ridge report by Cristy and Eckerman [(1987)]. These models are based on previous work by Snyder et al. [(1978)] and Cristy [(1980)], and were developed for calculations of doses absorbed in specific organs due to a source in some other organ. . . . A later report by Eckerman, Cristy, and Ryman [(1996)] added a description for the esophagus for the several ages and modified the head and neck descriptions to include a distinct neck region.

The Cristy and Eckerman models are presented as quadratic and planar equations for the organ surfaces. Specifications are given for the elemental composition of three tissue types: lung, skeletal, and soft tissue. The soft tissue composition is used for all organs other than the skeleton and lungs. All soft tissue organs thus appear the same to a radiation transport simulation. Unless a soft tissue organ is required as a source or a tally volume, the efficiency of a Monte Carlo transport simulation is improved by the omission of those organs and the filling of their volume by the generic trunk soft tissue.

[9] The text in square brackets represents our modifications to the model described by Staelens et al. (2003). Other details of our model incorporate proprietary information furnished by Philips Medical Systems.

A 21-year old male phantom was used for the present analysis. A semi-transparent 3-D view of this phantom is shown in Figure 2-3.

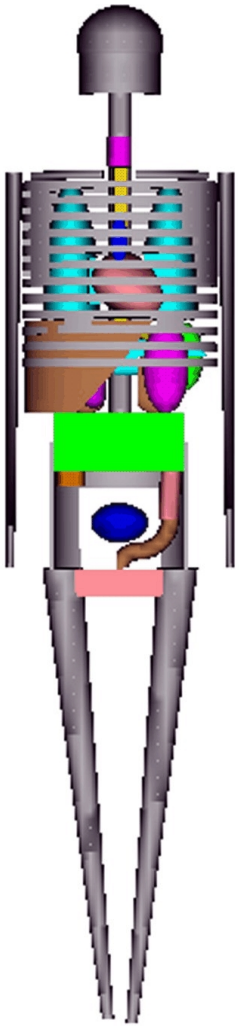

Figure 2-3. BodyBuilder Phantom of Adult Male

Room Model

A simplified geometry was used to describe the room containing the camera and the phantom. The room was modeled as a right circular cylinder room with 30-cm-thick concrete walls, floor, and ceiling. It is 3 m high, has a radius of 5 m, and is filled with moist air.

2.2 Method of Calculation

The MCNP simulation of the response of the gamma camera to a given source proceeds by a series of steps. First, a photon is emitted from a location within the source region (e.g., the lungs of the phantom) that is randomly selected by a scheme that ensures uniform sampling within the region. The energy of the photon is sampled from a probability distribution derived from the photon spectrum of the given radionuclide. The initial direction is sampled from an isotropic distribution.

The photon then interacts with the various materials (e.g., tissues within the phantom, components of the gamma camera, the concrete room, and the air filling the surrounding space). The interactions of primary interest in the range of photon energies in the present analysis include photoionization and Compton scattering, and, to a lesser extent, coherent scattering and pair production. The process continues until all of the energy of the initial photon is absorbed. Any energy deposited in the volume of space defined by the NaI crystal is assumed to produce a scintillation that is detected by the PMTs.

2.2.1 Photon Spectra of Radionuclides

The complete decay schemes of the four radionuclides in the present study are part of the DECDC decay data (JAERI 2001), that were prepared using decay data sets from the August 1997 version of the Evaluated Nuclear Structure Data Files (ENSDF). Included in these data sets are the energies and relative intensities of γ rays, x rays, annihilation quanta, Auger electrons, internal conversion electrons, and spontaneous fission, as well as detailed β-ray spectra. The spectra used as input to the MCNP calculations were selected from the tabulated photon spectra (γ rays and x rays). For three of the nuclides in the present study—^{60}Co, ^{192}Ir, and ^{241}Am—the selected spectra encompass over 99.9% of the total photon intensity of each nuclide.

In the case of ^{137}Cs, only the principal γ ray, with an energy of 661.66 keV, was included. The remainder of the photon spectrum comprises x rays with energies between 32 and 37 keV.

These energies would be excluded by any energy window of the Philips AXIS camera that was adjusted to count the photopeak energy of 662 keV.[10]

A summary of the photon spectra used in the present analysis is presented in Table 2-1.

Table 2-1. Spectra of Radionuclides in Present Study

Nuclide	Peak Energy[a] (keV)	Number of Spectral Lines[b]	Energy Range[c] (keV)	Total Intensity[d] (%)
Co-60	1173.24, 1332.5	2	1173.24 – 1332.5	199.9592
Cs-137	661.66	1	661.66 – 661.66	85.1
Ir-192	316.508	49	10.176 – 1061.48	233.624
Am-241	59.541	20	11.887 – 102.98	102.6

[a] Energy of photon emissions with maximum intensity

[b] Number of distinct photon energies included in calculations

[c] Range of photon energies included in calculations, not to be confused with energy window settings on gamma camera

[d] Total intensity of photon emissions included in calculations

2.2.2 Gaussian Energy Distribution

Energy deposited in the NaI(Tl) crystal produces a scintillation which in turn generates an electrical pulse in the camera system. The inherent statistics of the underlying ionization process and of the conversion of deposited energy to light produce a Gaussian broadening of the photopeak. This process cannot be explicitly modeled in standard Monte Carlo codes. Instead, a Gaussian energy-broadening treatment was applied to the pulse height distribution to account for the resolution of the gamma camera detectors. This is a feature of the MCNP5 code that approximates the broadening of the spectrum with a Gaussian function with a full width at half maximum (FWHM) that is a function of the energy (LANL 2004b):

$$F(E) = a\sqrt{E + b\,E^2}$$

F(E) = FWHM (MeV)

a = 0.0348767 ($MeV^{1/2}$)

b = 0.30486 (MeV^{-1})

E = energy (MeV)

The value of *b* used in the analysis is typical of NaI(Tl) detectors. The value of *a* was adjusted to yield a value of $\frac{F(E)}{E} = 0.095$ for E = 0.1405 MeV, the energy-dependent spectral resolution of the AXIS system (9.5% at 140.5 keV), as stated by the manufacturer (Staelens et al. 2003).

[10] See the discussion of energy windows in Section 2.4.1.

2.3 Validation of Model Using Field Measurements

The computer model was validated by comparing the results with measurements on the Philips AXIS camera presented in Chapter 1. Three of the sources used in the measurements selected for the comparison had nominal activities of 1 μCi (37 kBq), while ^{192}Ir had an activity 18.2 μCi (673 kBq).

MCNP simulations were performed that replicated the geometries of the measurements of count rates from discrete sources of four radionuclides in air at selected distances from the detector. The configurations of the sources were modeled upon the dimensions and materials described in Section 1.2.2 and illustrated in Figures 1-5 to 1-7. Both heads of the gamma camera were included in the model. Although only the first head was used to accumulate counts in these simulations, the second head, placed in the same position as during the measurement, potentially contributed to the backscattered photons reaching the first detector.

The calculations utilized the MCNP pulse height tallies, which record the detector events that fall into specified energy bins, such as those corresponding to the energy windows displayed in Table 2-2. The results are recorded as count per photon, and represent the probability that a photon emitted by the source would produce a pulse within the specified energy range. A more detailed explanation is presented in LANL 2004b:

> The pulse height tally provides the energy distribution of pulses created in a cell that models a physical detector. It also can provide the energy deposition in a cell. . . . The pulse height tally is analogous to a physical detector. The . . . energy bins correspond to the total energy deposited in a detector in the specified channels by each physical particle.
>
> In an experimental configuration, suppose a source emits 100 photons at 10 MeV, and ten of these get to the detector cell. Further, suppose that the first photon (and any of its progeny created in the cell) deposits 1 keV in the detector before escaping, the second deposits 2 keV, and so on up to the tenth photon which deposits 10 keV. Then the pulse height measurement at the detector would be one pulse in the 1 keV energy bin, 1 pulse in the 2 keV energy bin, and so on up to 1 pulse in the 10 keV bin.

The results of the comparison are shown in Table 2-2. The fifth column of this table lists the normalized count rates (expressed in cpm/nCi) derived from the measurements. These count rates were converted to counts per photon by first converting the units to counts/s per Bq and then dividing by the number of photons per disintegration, listed in the last column of Table 2-1.

The results of the comparison in Table 2-2 show good agreement in most cases. The agreement with the ^{60}Co measurements is particularly significant, since the count rates are based mostly on secondary radiation—primarily Compton scatter and, to a lesser extent, the annihilation quanta resulting from pair production—because the energy windows used in the measurements exclude the principal γ rays. This result indicates that the components of the camera which contribute significantly to the scatter, primarily the lead alloy shields around the detector, were modeled realistically.

Table 2-2. Comparison of Measured vs. Calculated Count Rates

Nuclide	Energy Window[a] (keV)	Distance (cm)	Measurements		MCNP Model	Difference (%)
			cpm/nCi	count/photon	count/photon	
Co-60	1.0 – 3.0	16.8	181.7	0.04094	0.04133	-0.96%
		29.5	97.7	0.02202	0.02110	4.17%
Cs-137	1.8 – 2.2	10	149.1	0.07890	0.07897	-0.08%
		22.6	70.0	0.03703	0.03773	-1.90%
		41.5	29.8	0.01577	0.01589	-0.78%
Ir-192	255.5 – 766.5	4.1	559.4	0.10785	0.17951	-66.44%
		16.8	397.3	0.07659	0.09255	-20.83%
		29.5	242.3	0.04673	0.04894	-4.73%
Am-241	40.5 – 121.5	16.8	153.1	0.06720	0.06785	-0.97%
		29.5	86.9	0.03813	0.03853	-1.04%

[a] The same energy windows were used in the MCNP simulations as in the measurements.

The ^{137}Cs calculations agree very well with the measured values. This agreement is enhanced by the 20% (i.e., ± 10%) window centered on the photopeak, which excludes incoherently scattered radiation. The calculation is thus dependent on the detailed geometry of crystal and the entrance window, but not on the other components of the camera and the surrounding structures. The ^{241}Am comparison also shows excellent agreement; again, the energy window spanned the primary photopeak. Although the energy window is wider in this case, virtually all of the relatively low-energy primary photons would be absorbed by the crystal, minimizing the contribution of scattered radiation.

The poor agreement for the ^{192}Ir source is due to the very high count rates experienced by the camera system. This source, which had an activity of 18.2 µCi, produced count rates in the range of $10^6 – 10^7$ cpm, which result in significant dead-time losses. The greatest discrepancy occurs when the source was closest to the crystal, producing the highest count rate. As the distance from the crystal increases, the count rate decreases and so does the discrepancy.

The lead alloy collimator used with the Philips AXIS camera could not be successfully modeled. Although MCNP can create a lattice of quadrilateral or hexagonal cells, this feature could not be used to replicate the actual structure of the AXIS collimator. Staelens et al. (2003) observed that the septa forming the hexagonal honeycomb are not uniform, being twice as thick in the horizontal direction as along the two diagonals, as shown in Figure 2-4. Since MCNP could not readily replicate this irregular geometry, we attempted to create an equivalent structure, constructing two collimator models using uniform hexagonal lattices. The first had septa with the thickness specified by Philips. In the second model, the additional thickness in the horizontal direction reported by Staelens et al. was distributed over all sides of the hexagonal cell, resulting in septa that were one third thicker than the manufacturer's specification. Neither model produced results that agreed with the

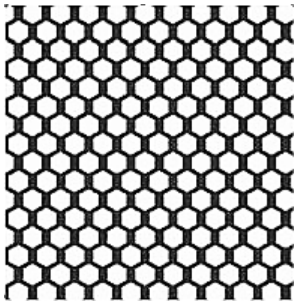

Figure 2-4. Details of Collimator (Staelens et al. 2003)

experimental measurements. Therefore, the remaining studies were limited to cameras without collimators.

2.4 Phantom Studies

The computer model was used to develop calibration factors for two models of the Philips AXIS camera: one equipped with a ¾-inch (1.9-cm) thick NaI crystal (the model used in the Hershey Medical Center studies), another with a ⅜-inch (0.95-cm) thick crystal. The two models are similar in design; however, the different detectors have different responses to incident radiation, especially for high energy γ rays that are not fully absorbed by the crystals.

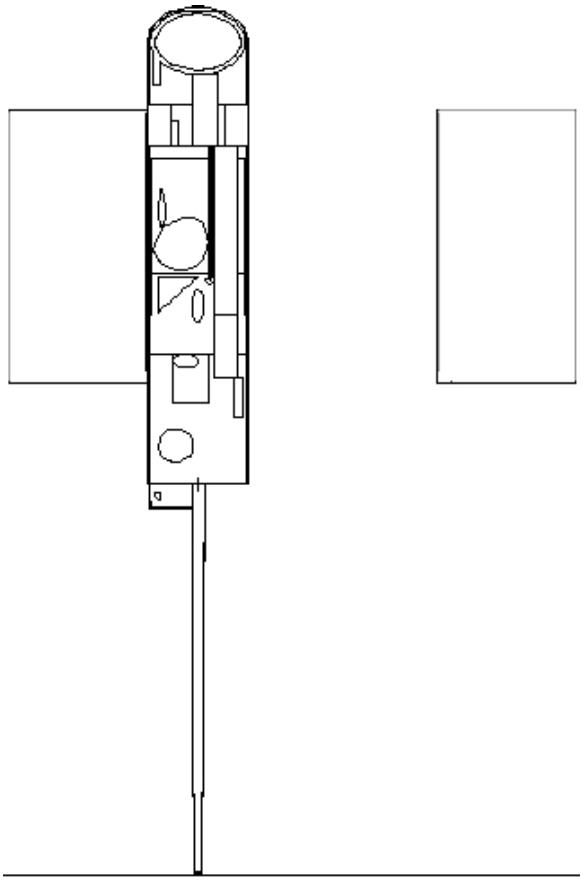

Figure 2-5. Sagittal Section of Phantom Facing Camera

The radioactive source was assumed to be uniformly distributed in the lungs of the anthropomorphic phantom described on page 2-3. As illustrated in Figures 2-5 and 2-6, the phantom was positioned facing the camera, with the chest wall immediately adjacent to the edges of the lead shield and consequently 2 cm from the front of the aluminum window that covers the detector. This position represents the normal position of a patient undergoing a lung scan, except for the absence of the collimator. The second head, not used to collect counts in this simulation, was positioned behind the phantom, aligned with the first head. This head would most likely be in such a position during the assessment of an exposed individual and, as mentioned previously, could contribute to backscatter. Figure 2-7 illustrates the position of the phantom and the camera in the room described on page 2-4.

2.4.1 Derivation of Calibration Factors

As is discussed in Section 1.2.3, the operator of the gamma camera can select one of a number of preset energy windows. In addition, both the window width and the energy peak can be adjusted for a particular study. However, there are certain limits on the settings of energy windows on the AXIS camera, as explained in Section 1.2.3. For the widest window, the so-called "200%" window, the lowest energy in the range falls into Channel 25 of the pulse height analyzer, while the highest energy corresponds to Channel 231. Thus the energy range is represented by the quotient 231 ÷ 25 = 9.24, the ratio of the highest and lowest energies in the range.

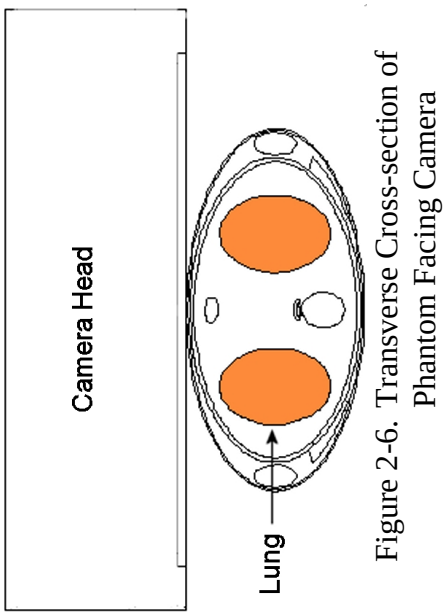

Figure 2-6. Transverse Cross-section of Phantom Facing Camera

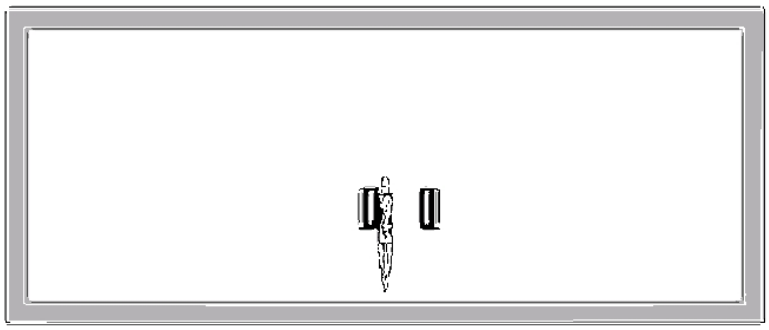

Figure 2-7. Phantom in Concrete Room Facing Camera

In principle, the highest count rate from a given source would be obtained by using the widest window spanning the appropriate energy range. In actual practice, a better signal-to-noise ratio might be achieved by using a narrower window which would reduce the background. Comprehensive data on background counts over the entire range of possible energy windows were not acquired in the course of the present study; background radiation was not considered in developing optimum energy windows in the present analysis.

To determine the optimum energy window, as well as to calculate the count rates from alternate windows that might be selected by the operator of the AXIS camera, we calculated MCNP pulse height tallies over the entire range of energies that could be recorded by the camera. These tallies were sorted by energy at increments of 1 keV, producing an array of 1-keV-wide energy bins. An example of such a spectrum, including the effect of the Gaussian energy broadening described in Section 2.2.2, is shown in Figure 2-8.

The analysis of these data comprised the following steps. The lowest energy channel that could be set on the AXIS camera is 7 keV. Thus the lowest "200%" window spans the range of 7 – 64.68 keV (7 × 9.24 = 64.68). We approximated the count rate in this window by summing the counts in bins in the range of 7 – 65 keV.[11] We next repeated this process for the range 8 – 74 keV (8 × 9.24 = 73.92), continuing stepwise until the upper end of the range corresponded to the highest energy bin in the pulse height spectrum of the given radionuclide. We then compared the summed counts in all these energy ranges and selected the one with the highest counts, which represents the optimum energy window for the given combination of radionuclide and detector in the given exposure geometry. In the example shown in Figure 2-8, the optimum window encompasses both photopeaks and most of the pulses from the Compton-scattered photons.

[11] Each bin is designated by the upper bound of its energy range. Thus, the 7 keV bin registers counts over the range of 6 – 7 keV and has an average energy of 6.5 keV.

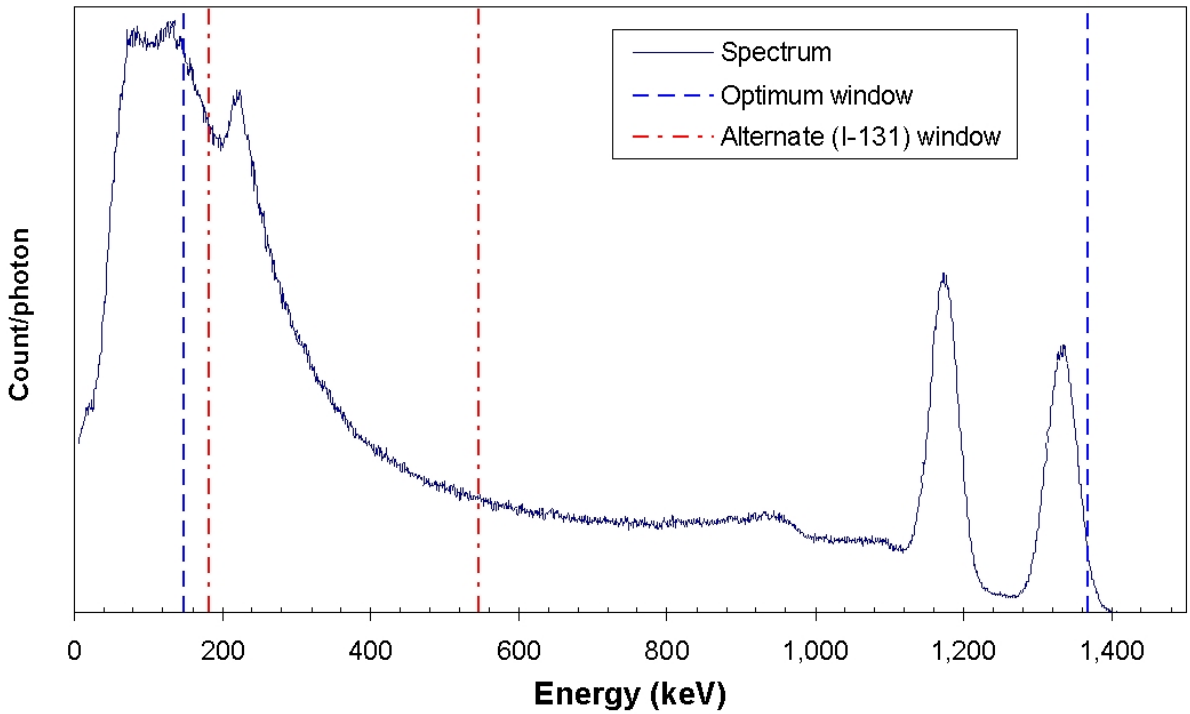

Figure 2-8. Pulse Height Spectrum of ^{60}Co Distributed in Lungs, Showing Energy Windows

A similar process was used to select an alternate energy window for each radionuclide-detector combination. These windows are based on factory-preset radionuclide windows, expanded to a width of 100% (i.e., 50 – 150% of the peak energy). Thus, the highest and lowest energies within a given 100% window have a ratio of 3:1. Again, the selected alternate window is the one that would yield the highest count rate, based on the MCNP pulse height tallies. The optimum and alternate energy windows for each radionuclide and each model of the AXIS camera are listed in Table 2-3. The last column of the table lists the calibration factor, in cpm/nCi, for each energy window. The relationship between these normalized count rates and the counts/photon listed in the next-to-last column is explained on page 2-6.

2.4.2 Comparison of Mathematical Phantom with Measurements on Acrylic Slab Phantom

The normalized count rates derived from the MCNP simulations may be compared to the measurements made on the AXIS camera with a ¾-inch crystal and no collimator, with the sources at different depths inside the acrylic slab phantom, which are reproduced in Table 2-4. Because most of the measurements used different energy windows than those utilized by the calculations reported in Table 2-3, the results would be expected to differ. To enable a direct comparison, we calculated the normalized count rates for the windows used in the measurements, based on the pulse height tallies described in Section 2.4.1; the results are presented in Table 2-4.

Table 2-3. Calibration Factors for AXIS Camera Using Various Energy Windows

Nuclide	Crystal[a] (in)	Window				Count/ photon	cpm/nCi
		Designation	Peak Energy (keV)	Width (%)	Energy Range (keV)		
Co-60	0.75	Optimum	650.7	200	147.5 – 1367.0	0.1331	591
		I-131	364.5	100	182.3 – 546.8	0.0626	278
	0.375	Optimum	311.9	200	70.5 – 655.5	0.0975	433
		I-123	159.0	100	79.5 – 238.5	0.0587	261
Cs-137	0.75	Optimum	329.5	200	74.5 – 692.5	0.1907	360
		F-18	511.0	100	255.5 – 766.5	0.0928	175
	0.375	Optimum	325.1	200	73.5 – 683.3	0.1507	285
		I-123	159.0	100	79.5 – 238.5	0.0884	167
Ir-192	0.75	Optimum	232.7	200	52.5 – 489.2	0.2201	1142
		I-123	159.0	100	79.5 – 238.5	0.1176	610
	0.375	Optimum	166.7	200	37.5 – 350.6	0.1916	994
		I-123	159.0	100	79.5 – 238.5	0.1129	586
Am-241	0.75	Optimum	34.7	200	7.5 – 73.4	0.0556	127
		Xe-133	81.0	100	40.5 – 121.5	0.0433	99
	0.375	Optimum	34.7	200	7.5 – 73.4	0.0556	127
		Xe-133	81.0	100	40.5 – 121.5	0.0433	99

[a] Nominal thickness of NaI crystal

Table 2-4. Comparison of Measured Count Rates from Acrylic Phantom with MCNP Simulations of Mathematical Phantom

Nuclide	Window	Count rate (cpm/nCi)			
	Energy Range (keV)	Measured in Acrylic Phantom			Calculated
		Depth (cm): 2.4	4.8	7.1	
Co-60	330.8 – 992.5	304	253.0	211	233
Cs-137	595.5 – 727.8	109	71	48	67
Ir-192	255.5 – 766.5	454	361	278	403
Am-241	40.5 – 121.5	207	131	85	99

As shown in Table 2-4, the normalized count rates based on activities uniformly distributed in the lungs of the mathematical phantom are bracketed by the results measured with discrete sources at depths of 4.8 and 7.1 cm inside the acrylic phantom for all the nuclides except ^{192}Ir. The calculated count rate for ^{192}Ir is higher than the normalized count rate at 4.8 cm, due to the dead-time losses from the high count rates, as discussed previously.

2.5 Conclusions

Several conclusions can be drawn from this analysis. The Philips AXIS cameras, used with the optimum 200% windows listed in Table 2-3, yield the highest sensitivity for detecting activities in the lungs of an exposed individual. These settings yield higher count rates than would windows based on preset radionuclides, including those used in the measurements on the acrylic phantoms.

The AXIS camera with the ¾-inch crystal has significantly greater sensitivities than the thinner crystal to nuclides with the highest energy γ-ray emissions, namely ^{60}Co and ^{137}Cs. This is expected, since neither crystal fully absorbs these high-energy photons. The difference is less significant for the medium-energy emissions from ^{192}Ir and vanishes for ^{241}Am. The low-energy principal γ ray from the latter nuclide is almost completely absorbed by either crystal.

As demonstrated by the discrepancy between the measured count rates from the high-activity ^{192}Ir source and calculated values, dead-time losses need to be accounted for in developing protocols for assessing exposed individuals. This issue will be addressed in future studies of the use of hospital radiation detection instruments in performing such assessments.

These studies also demonstrate that the MCNP calculations can serve as a good surrogate for estimating the responses of different models of gamma cameras. Since, in addition to the phantom of an adult male used in the present simulations, the BodyBuilder program can generate phantoms for different ages, both sexes, and obese individuals, the analytical methodology described in this chapter can also be used to generate calibration factors for a wide range of exposed individuals.

The results presented in Section 2.4.2 support the derivation of provisional calibration factors for the thyroid uptake monitor and the portal monitor, based on the response of these instruments to discrete sources at selected depths within the acrylic slab phantom. The provisional calibration factors for these instruments are discussed in Section 1.6.

Finally, as was discussed in Section 1.7, the calibration factors presented in this report apply only to activities in the lungs at the time of the measurement. They do not account for the clearance of radionuclides from the lungs following inhalation, nor for contributions to the count rate from radionuclides that have migrated to other organs or tissues. The estimate of activities in the lungs based on the count rates in the detectors is not a sufficient basis for performing a radiological assessment of the exposed individual without accounting for these additional factors.

References

Cristy, M. 1980. "Mathematical Phantoms Representing Children of Various Ages for Use in Estimates of Internal Dose," NUREG/CR-1159. Washington, DC: U.S. Nuclear Regulatory Commission.

Cristy, M., and K. F. Eckerman. 1987. "Specific Absorbed Fractions of Energy at Various Ages from Internal Photon Sources. I. Methods," ORNL/TM-8381/V1. Oak Ridge, TN: Oak Ridge National Laboratory.

Eckerman, K. F. M. Cristy, and J. C. Ryman. 1996. "The ORNL Mathematical Phantom Series." <http://homer.hsr.ornl.gov/VLab/mird2.pdf> (October 21, 2005).

International Commission on Radiological Protection (ICRP). 1996. "Conversion Coefficients for use in Radiological Protection against External Radiation," ICRP Publication 74. *Annals of the ICRP*, *26* (3/4). Tarrytown, NY: Elsevier Science, Inc.

Los Alamos National Laboratory (LANL). 2004a. MCNP5: Monte Carlo N-Particle Transport Code System, Version 1.30, RSICC Code Package CCC-710 [Computer software and manual]. Oak Ridge, TN: Oak Ridge National Laboratory.

Los Alamos National Laboratory (LANL), X-5 Monte Carlo Team, Diagnostics Applications Group. 2004b. "MCNP - A General Monte Carlo N-Particle Transport Code, Version 5." <http://www-xdiv.lanl.gov/x5/MCNP/pdf/MCNP5_manual_VOL_I.pdf> (October 21, 2005)

Snyder, W. S., M. R. Ford, and G. G. Warner. 1978. "Estimates of Specific Absorbed Fractions for Photon Sources Uniformly Distributed in Various Organs of a Heterogeneous Phantom," MIRD Pamphlet No. 5, Revised. New York: Society of Nuclear Medicine.

Staelens et al. 2003. "Monte Carlo Simulations of a Scintillation Camera Using GATE: Validation and Application Modelling." *Phys. Med. Biol. 48*, 3021-3042. <https://archive.ugent.be/retrieve/1264/lemahieu1.pdf> (October 31, 2005)

Tokai Research Establishment, JAERI. 2001. DECDC 1.0: Nuclear Decay Data Files for Radiation Dosimetry Calculations, DLC-213, RSICC Data Library Collection [Computer software and manual]. Oak Ridge, TN: Oak Ridge National Laboratory.

Van Riper, K. A. 2004. "BodyBuilder: A Product of White Rock Science." <http://www.whiterockscience.com/bodybuilder/oakridge.html> (October 21, 2005)

White Rock Science. 2004. BodyBuilder (Version 1.30) [Computer software and manual]. Los Alamos, NM: Author.